THE UNIVERSITY OF
WARWICK

# Library Declaration and Deposit Agreement

1. **STUDENT DETAILS**

   Nelson Yeung
   1023743

2. **THESIS DEPOSIT**

   2.1 I understand that under my registration at the University, I am required to deposit my thesis with the University in BOTH hard copy and in digital format. The digital version should normally be saved as a single pdf file.

   2.2 The hard copy will be housed in the University Library. The digital version will be deposited in the Universitys Institutional Repository (WRAP). Unless otherwise indicated (see 2.3 below) this will be made openly accessible on the Internet and will be supplied to the British Library to be made available online via its Electronic Theses Online Service (EThOS) service. [At present, theses submitted for a Masters degree by Research (MA, MSc, LLM, MS or MMedSci) are not being deposited in WRAP and not being made available via EthOS. This may change in future.]

   2.3 In exceptional circumstances, the Chair of the Board of Graduate Studies may grant permission for an embargo to be placed on public access to the hard copy thesis for a limited period. It is also possible to apply separately for an embargo on the digital version. (Further information is available in the Guide to Examinations for Higher Degrees by Research.)

   2.4 (a) Hard Copy I hereby deposit a hard copy of my thesis in the University Library to be made publicly available to readers immediately.
   I agree that my thesis may be photocopied.

   (b) Digital Copy I hereby deposit a digital copy of my thesis to be held in WRAP and made available via EThOS.
   My thesis can be made publicly available online.

3. **GRANTING OF NON-EXCLUSIVE RIGHTS**

Whether I deposit my Work personally or through an assistant or other agent, I agree to the following: Rights granted to the University of Warwick and the British Library and the user of the thesis through this agreement are non-exclusive. I retain all rights in the thesis in its present version or future versions. I agree that the institutional repository administrators and the British Library or their agents may, without changing content, digitise and migrate the thesis to any medium or format for the purpose of future preservation and accessibility.

4. **DECLARATIONS**

(a) I DECLARE THAT:

- I am the author and owner of the copyright in the thesis and/or I have the authority of the authors and owners of the copyright in the thesis to make this agreement. Reproduction of any part of this thesis for teaching or in academic or other forms of publication is subject to the normal limitations on the use of copyrighted materials and to the proper and full acknowledgement of its source.
- The digital version of the thesis I am supplying is the same version as the final, hardbound copy submitted in completion of my degree, once any minor corrections have been completed.
- I have exercised reasonable care to ensure that the thesis is original, and does not to the best of my knowledge break any UK law or other Intellectual Property Right, or contain any confidential material.
- I understand that, through the medium of the Internet, files will be available to automated agents, and may be searched and copied by, for example, text mining and plagiarism detection software.

(b) IF I HAVE AGREED (in Section 2 above) TO MAKE MY THESIS PUBLICLY AVAILABLE DIGITALLY, I ALSO DECLARE THAT:

- I grant the University of Warwick and the British Library a licence to make available on the Internet the thesis in digitised format through the Institutional Repository and through the British Library via the EThOS service.
- If my thesis does include any substantial subsidiary material owned by third-party copyright holders, I have sought and obtained permission to include it in any version of my thesis available in digital format and that this permission encompasses the rights that I have granted to the University of Warwick and to the British Library.

5. **LEGAL INFRINGEMENTS**

I understand that neither the University of Warwick nor the British Library have any obligation to take legal action on behalf of myself, or other rights holders, in the event of infringement of intellectual property rights, breach of contract or of any other right, in the thesis.

---

*Please sign this agreement and return it to the Graduate School Office when you submit your thesis.*

Student's signature: .....Date: .....

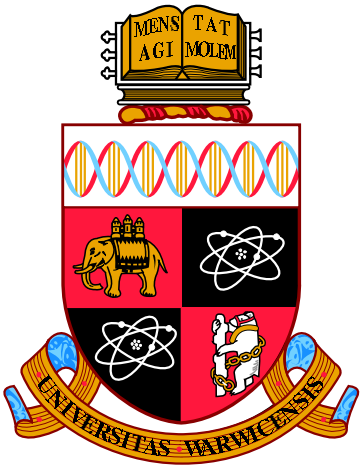


# A Density Functional Theory Study of the Effects of Compositional Disorder on "Half-Metallic" Spintronics Materials

by

**Nelson Yeung**

**Thesis**

Submitted to the University of Warwick

for the degree of

**Master of Science (by research)**

**Department of Physics**

March 2015

THE UNIVERSITY OF WARWICK

# Contents

# List of Figures

# Acknowledgments

I would like to pay special thanks to Prof. J. B. Staunton for her wise supervision throughout my MRes studies, not only that but also for supporting me with my job hunting. I am also very grateful to Dr. G. Bell and the half-metals team at York university for providing me some insights into experimental work being done. My thoughts also go to my friends, too many to be named, but in particular, Jamie, who had helped me to solve many physics and computational problems. I would also like to mention my officemates two Alexes, who have been enjoyable, if not time wasting company over the whole year.

The financial support from the Barclays bank is gratefully acknowledged. I must also thank the Physics Department and the Centre for Scientific Computing at the University of Warwick for providing computing resources, without them all this work would not have been possible. Above all, however, I thank my parents for their support—financially, physically and mentally—studying at a university is simply impossible without them.

# Declarations

This thesis is submitted to the University of Warwick as my application towards the degree of Master of Research, and presents details of research carried out in the Theory Group of the Department of Physics between October 2013 and September 2014. The content of this thesis is my own work, unless stated otherwise, carried out under the supervision of Prof. J. B. Staunton. No part of this thesis has previously been submitted for a research degree at any other institution.

# Abstract

This thesis presents the results of a detailed analysis of the half-metallicity of the $B2$ $CoFe_xMn_{0.5-x}Ga_ySi_{0.5-y}$ ($0 < x < 0.5$, $0 < y < 0.5$) alloys. Using the Korringa-Kohn-Rostoker method with the coherent potential approximation (KKR-CPA), the electronic density of states (DOS) and Bloch spectral functions (BSFs), which represent the $\epsilon$–$\mathbf{k}$ dispersion relations in disordered alloys, are calculated. We propose methods of quantifying the half-metallicity using information from the DOS and BSF, which is applied to 5-component alloys. The analysis of the DOS involves the calculation of the number of states around the Fermi level and the spin up-spin down DOS difference at the Fermi level. From the BSF, the Fermi velocity and the mean free path of the electrons is extracted. The combined results of the analyses have shown that candidates for potential half-metals are among the ones that have low Fe and Ga concentrations. The result also indicates that the half-metallicity of the alloys is more sensitive to the increase of the Fe concentration, where it drops more rapidly, compared with the increase of Ga concentration.

# Chapter 1

# Introduction

The theory of electrical conductivity has over a 100 years of history [1]. In the beginning, the description of conduction was based on classical kinetic theory [2]. It was indeed very successful in describing conductivity in metals. The sole use of classical theory, however, does not give an accurate picture of the charge carriers and has proven to have many problems [2]. For example, the phenomenon of semi-conduction cannot simply be explained through classical theory, as the idea of valence and conduction electrons is non-existent. The advent of quantum mechanics later shed light on the theory of metallic conduction. The recognition of electron spin and how conduction can be different depending on these spins allowed phenomena such as half-metallicity. The heart of this thesis is the study of half-metallic materials, thus quantum mechanics will constitute the pillar of the whole thesis.

Half-metallic materials or half-metals (HMs) are compounds for which only one of the spin channels presents a conducting behaviour for the electrons while the other spin channel is insulating [3]. This property is caused by the presence of a band gap at the Fermi level, $\epsilon_f$ only for one spin channel, this spin channel is therefore an insulator or a semiconductor. This also leads to 100% spin polarisation at $\epsilon_f$ for the other spin channel, meaning that all HM are also ferromagnetic or ferrimagnetic [3]. These materials were predicted theoretically in the 1980's [4], since then they have attracted significant amount of attention [5] because of their potential applications in spintronics (e.g., magnetic random access memory (MRAM), decrease in power consumption and increase in data processing speed compared to conventional electronic devices [6, 7]).

The most notable examples of potential HMs are oxides, sulphides and Heusler alloys [8]. Although many materials were predicted to be HM, demonstrating experimentally their half-metallicity has been shown to be tremendously

difficult due to the effects of, structural disorder [9], for example. Though indeed, experimental work has yet to demonstrate true HM behaviour, many materials have been found that have a high spin polarisation at $\epsilon_f$ [10]. Geiersbach *et al.* [11] found that the electrical conductivity is quite low for (1 1 0) thin films of Co-based Heusler alloys grown on top of a MgO (1 0 0) substrate, indicating structural disorder. The study of disordered alloys is therefore of paramount importance. This thesis is mainly concerned with the partially disordered $B2$ structure and the effects of compositional disorder on HM. Moreover, the Co-based Heusler and $B2$ alloys are of our primary interests, as they exhibit Curie temperatures well above room temperature [10] which is important for spintronic applications.

To study the properties of the HM, simple models can be deployed, where the many-body Hamiltonian is simplified with specific parameters, but for a more independent and quantitative analysis, a first-principles approach is needed. There are several first-principles quantum mechanical approaches, but the most noteworthy, successful in both accuracy and computational expediency, is density functional theory (DFT) [12]. DFT is a computational method that maps the complicated many-body problem onto a Kohn-Sham (KS) non-interacting system [13]. The resulting one electron equations from DFT can be solved using multiple scattering theory (MST), the Korringa-Kohn-Rosoker (KKR) Green function (GF) method [14]. This method was chosen on the basis of the fact that it can be generalised easily with the coherent potential approximation (CPA), which can deal with disorder. This is crucial, as we are mainly dealing with disordered systems. These calculations are carried out using Munich SPRKKR package [15, 16], which was extensively used in the present work.

We begin, in Chapter 2, by introducing the calculations behind DFT and the use of the local density approximation (LDA) to specify a one electron exchange-correlation potential. Then the method of using GF and MST to provide practical solutions to the DFT equations is presented. The implementation of CPA with MST to deal with substitutional disorder is then outlined.

With the calculations and theories forming the backbone of this thesis presented, we then detail the concepts of HM and Heusler alloys in Chapter 3. Following the discussion of ferromagnetism in HM, we present DFT calculations of Cobalt in the simple hexagonal close-packed (HCP) and face-centered cubic (FCC) structures, in order to demonstrate ferromagnetism. We end the chapter with the study of the well-known Heusler alloy $L2_1$ $Co_2MnSi$, and its $B2$ structure, $CoMn_{0.5}Si_{0.5}$.

Chapter 4 is where we begin the analysis of the alloy of our interest, the $B2$ $CoFe_xMn_{0.5-x}Ga_ySi_{0.5-y}$ system. This chapter concentrates on studying the half-

metallicity through the density of states (DOS), where the method of analysing the band gap and DOS difference at $\epsilon_f$ is presented. Some of the main achievements of this thesis through the analysis is also presented here.

We review in Chapter 5 the attempt to look beyond just the DOS and investigate the transport properties. Theory of transport properties of solids, namely the Boltzmann transport equation is detailed here. The calculations of Bloch spectral function (BSF) using GF and its relationship with the band structure is then presented. The extraction of the Fermi velocity and the mean free path of an electron through the BSF is shown and the $B2$ $CoFe_xMn_{0.5-x}Ga_ySi_{0.5-y}$ is again looked at with the two new analysis. The chapter ends with the final main achievements of this thesis. Final conclusions concerning the main findings and an outlook then conclude this thesis.

# Chapter 2

# *Ab-initio* Theory of Electronic Structure

## 2.1 Density functional theory

To study a solid state system, one can consider the Hamiltonian for a system of interacting electrons [17],

$$\hat{H} = \hat{K} + \hat{V} + \hat{U} = -\frac{1}{2}\sum_i \nabla_i^2 + \sum_i V_{ext}(\mathbf{r}_i) + \frac{1}{2}\sum_i \sum_{j\neq i} \frac{1}{|\mathbf{r}_i - \mathbf{r}_j|}. \tag{2.1}$$

This is written in terms of Hartree atomic units, where $m_e = \hbar = e = 1/4\pi\epsilon_0 = 1$. The $V_{ext}$ term is some external potential, which can be included to incorporate the effect of fixed nuclei. However, since a material contains more than a septillion electrons interacting with each other, solving the Schrödinger equation with such Hamiltonian is almost impossible. Instead, density functional theory (DFT) can be used. It maps this complicated many electron Hamiltonian onto an effective one electron Hamiltonian.

Hohenberg and Kohn laid out the foundation of DFT, where they have proved two important theorems concerning the electronic density [18]. The first theorem states that some external potential $V_{ext}(\mathbf{r})$ is a unique functional of the ground state electron density, $n(\mathbf{r})$. In other words, $n(\mathbf{r})$ uniquely determines $V_{ext}(\mathbf{r})$ to within a constant. The second theorem states that the energy functional of a system for a given potential, $E[n_\uparrow, n_\downarrow]$ is minimised by $n(\mathbf{r})$. These are the original statements, which are sufficient for illustration purposes. Though, applicable extensions to less restrictive formulations and to degenerate ground states exist. It can be seen from these two theorems that DFT concentrates on describing the ground state properties

of interacting electron systems.

With these two theorems established, let us now consider the energy functional,

$$E[n_\uparrow, n_\downarrow] = \langle \Psi | \hat{K} + \hat{U} + \hat{V} | \Psi \rangle = \sum_\sigma \int V^\sigma_{ext}(\mathbf{r}) n^\sigma(\mathbf{r}) d\mathbf{r} + F[n_\uparrow, n_\downarrow], \tag{2.2}$$

where the summation is over all spins, $\sigma = \uparrow\downarrow$ and $F[n_\uparrow, n_\downarrow]$ is a universal functional that is valid for any external potential and number of particles. The exact form of this functional is unknown and therefore $E[n_\uparrow, n_\downarrow]$ still cannot be minimised as it is. However, by using a fictitious system as shown by Kohn and Sham [13], where interacting particles are replaced by non-interacting ones that generates the same density, $F[n_\uparrow, n_\downarrow]$ can be written as [13]

$$\begin{aligned} F[n_\uparrow, n_\downarrow] &= K_S + E_H + E_{xc} \\ &= \frac{1}{2} \sum_\sigma \sum_i^N |\nabla \phi^\sigma_i(\mathbf{r})|^2 + \frac{1}{2} \int d\mathbf{r} \int \frac{n(\mathbf{r}) n(\mathbf{r}')}{|\mathbf{r} - \mathbf{r}'|} d\mathbf{r}' + E_{xc}[n_\uparrow, n_\downarrow] \end{aligned} \tag{2.3}$$

The first term is the kinetic energy of the non-interacting system, the second term is known as the Hartree interaction energy, where electron-electron interaction is replaced by the average potential of the other electrons and the final term is the exchange-correlation energy containing all the many-body effects of exchange and correlation. By comparing Eq. (2.2) and Eq. (2.3), $E_{xc}$ can be written as

$$E_{xc} = F - (K_S + E_H) = K - K_s + U - E_H. \tag{2.4}$$

This is only a small contribution, but a good approximation for it is very vital for any accurate DFT calculations.

With $F[n_\uparrow, n_\downarrow]$ defined, $E[n_\uparrow, n_\downarrow]$ can now be minimised with respect to variations in $n(\mathbf{r})$, that is to solve the Euler-Lagrange equation, which gives

$$\left( -\frac{1}{2} \nabla^2 + V^\sigma_{eff}(\mathbf{r}) \right) \phi^\sigma_i(\mathbf{r}) = \epsilon^\sigma_i \phi^\sigma_i(\mathbf{r}). \tag{2.5}$$

This is known as Kohn-Sham (KS) equation, where $V^\sigma_{eff}$ is given by

$$V^\sigma_{eff}(\mathbf{r}) = V^\sigma_{ext}(\mathbf{r}) + V_H(\mathbf{r}) + V^\sigma_{xc}(\mathbf{r}). \tag{2.6}$$

From the Hartree interaction energy, the Hartree potential, $V_H(\mathbf{r})$ is given by

$$V_H(\mathbf{r}) = \int \frac{n(\mathbf{r}')}{|\mathbf{r} - \mathbf{r}'|} d\mathbf{r}' \tag{2.7}$$

and the exchange-correlation potential, $V_{xc}^{\sigma}(\mathbf{r})$ is defined as

$$V_{xc}^{\sigma}(\mathbf{r}) = \frac{\delta E_{xc}[n_\uparrow, n_\downarrow]}{\delta n_\sigma(\mathbf{r})}. \tag{2.8}$$

The form of $E_{xc}[n_\uparrow, n_\downarrow]$ is unknown except the most simple systems. Hence a numerical approximation is needed. For $n(\mathbf{r})$ varying slowly, the local density approximation (LDA) can be used. LDA assumes that the exchange-correlation energy density at each point in space is the same as in a homogeneous electron gas (HEG) having the same charge density as at the given point. This gives [19]

$$E_{xc}[n_\uparrow, n_\downarrow] = \int n(\mathbf{r}) \epsilon_{xc}^{HEG}(n_\uparrow, n_\downarrow) d\mathbf{r}. \tag{2.9}$$

Despite the local approximation, LDA is remarkably successful in describing the ground state properties of many real materials. The key for the success is mostly due to the fact that the approximation satisfies the sum rules for the exchange-correlation hole in the charge density [20]. However successful LDA is, it still has many limitations and net error [19] (See reference [12, 21] for a more in-depth review of the applications of the LDA to real systems and the DFT formulations).

If we now take the charge density from the Kohn-Sham approximation

$$n(\mathbf{r}) = \sum_i^N f_i \phi_i^*(\mathbf{r}) \phi_i(\mathbf{r}), \tag{2.10}$$

where $f_i$ the Fermi-Dirac distribution, it can be seen that the charge density depends on the effective potential and the effective potential depends on the charge density. This means that the charge density along with the KS equations is a set of closed equations and can be solved self-consistently.

## 2.2 Multiple Scattering Theory

Although with the KS equations, the problem is already much simpler than the original many-body problem, we are still left with a rather difficult eigenvalue problem to solve. Here, we will introduce the Korringa-Kohn-Rostoker (KKR) method, based on multiple scattering theory and the Green's functions (GF) formalism, which is

one way to find the solution to such equations [22, 23].

The GFs $G(z)$ and $G_0(z)$ with the corresponding Hamiltonian $H$ and $H_0$ respectively at complex energy $z = \epsilon + i\delta$, are defined as [24]

$$G(z) = (\epsilon - H + i\delta)^{-1} \ , \ \ G_0(z) = (\epsilon - H_0 + i\delta)^{-1}. \tag{2.11}$$

The density of state (DOS) of a system can be computed by considering the position representation of the GF,

$$G(\mathbf{r}, \mathbf{r}'; \epsilon) = \sum_i \frac{\psi_i(\mathbf{r})\psi_i^*(\mathbf{r}')}{\epsilon - \epsilon_i + i\delta}. \tag{2.12}$$

This can be rewritten using the identity [24]

$$\lim_{y \to 0^+} (x + iy)^{-1} = Px^{-1} - i\pi\delta(x) \tag{2.13}$$

as

$$G(\mathbf{r}, \mathbf{r}'; \epsilon) = \sum_i \frac{\psi_i(\mathbf{r})\psi_i^*(\mathbf{r}')}{\epsilon - \epsilon_i} + i\pi \sum_i \delta(\epsilon - \epsilon_i)\psi_i(\mathbf{r})\psi_i^*(\mathbf{r}'). \tag{2.14}$$

With this definition of GF, the DOS can be easily obtained by integrating the GF over $\mathbf{r}$ and taking the imaginary part, realising the quantity $\sum_i \delta(\epsilon - \epsilon_i)$ is the DOS at $\epsilon$, $n(\epsilon)$. This will arrive at the following relation,

$$-\frac{1}{\pi}\mathrm{Im\,Tr}\, G(\epsilon) = \sum_i \delta(\epsilon - \epsilon_i) = n(\epsilon), \tag{2.15}$$

where $G(\epsilon)$ is the spectral representation which can be obtained following the identity from Eq. (2.13). Using Eq. (2.10), the electron density can be written in terms of GF, giving

$$n(\mathbf{r}) = -\frac{1}{\pi}\mathrm{Im\,Tr} \int_{-\infty}^{\epsilon_f} f(\epsilon) G(\mathbf{r}, \mathbf{r}'; \epsilon) d\epsilon. \tag{2.16}$$

Since we are only dealing with the ground state, we can take the temperature $T = 0$, meaning that $f(\epsilon)$, the Fermi-Dirac distribution is simply $f(\epsilon) = 1$ for $\epsilon \leq \epsilon_f$ and zero otherwise.

From the KS equations, the problem is now only a single particle problem, so to begin the description of this multiple scattering approach, lets consider a simple single particle system with Hamiltonian $H$,

$$H\psi_i = \epsilon_i \psi_i \qquad \Rightarrow \qquad (\epsilon_i - H)\psi_i = 0. \tag{2.17}$$

Suppose that $H$ can be written as some perturbation $V$ in addition to an unperturbed Hamiltonian $H_0$ (i.e., $H = H_0 + V$), where $H_0$ has its own set of eigenfunctions $\phi_i$ and that the eigenfunctions $\psi_i$ can be written in terms of the unperturbed eigenfunctions $\phi_i$ with some change $\delta\psi_i$ (i.e., $\psi_i = \phi_i + \delta\psi_i$), we can write

$$(\epsilon_i - H)\delta\psi_i = V\phi_i. \tag{2.18}$$

Equating this with Eq. (2.11) will result in what is known as the Lippmann-Schwinger equation [25],

$$\psi_i = \phi_i + G(\epsilon_i)V\phi_i \ , \ \ \psi_i = G_0(\epsilon_i)V\psi_i. \tag{2.19}$$

This equation gives rise to a simple physical significant, that the final wavefunction is simply sum of the unperturbed wavefunction $\phi_i$ and the potential $V$ that describes the interaction between the colliding systems. Note that the small imaginary part, $\delta$ takes two limits $\delta \to \pm 0$ but for this discussion it was taken to be positive. Although it has no physical meaning, it will become apparent later on the necessity of this constant.

Going back to the definitions of the GFs, Eq. (2.11), one can write $G(z)$ in terms of $G_0(z)$ which gives,

$$\begin{aligned} G(z) &= \frac{1}{z - H} = \frac{1}{z - (H_0 + V)} \\ &= \frac{1}{z - H_0}\left(\frac{1}{1 - V(z - H_0)^{-1}}\right) \\ &= G_0(z)\sum_{n=0}^{\infty}\big(VG_0(z)\big)^n. \end{aligned} \tag{2.20}$$

This can be reformulated by defining an operator, the so-called *T-operator*,

$$T(z) = V\sum_{n=0}^{\infty}\big(G_0(z)V\big)^n = V + VG_0(z)T(z)\,, \tag{2.21}$$

such that

$$G(z) = G_0(z) + G_0(z)T(z)G_0(z). \tag{2.22}$$

This final expression is referred to as Dyson equation [26]. This *T-operator* contains all the effects of the scattering from the potential $V$. Using these definitions, the Lippmann-Schwinger equation can be rewritten as

$$\psi_i = \phi_i + G_0(\epsilon_i)T(\epsilon_i)\phi_i. \tag{2.23}$$

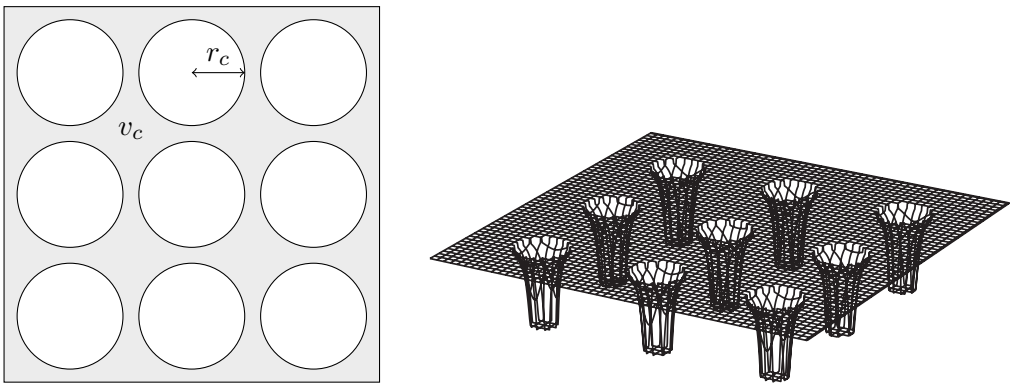


(a) (b)

Figure 2.1: Schematic diagrams of the muffin-tin potential. (a) A top-down view of the potential. The white circles represent the spherically symmetric potentials with a radius $r_c$ and the shaded area which are outside of $r_c$ have a constant potential $v_c$ (b) 3D view of the potential.

Let us now proceed to solve the multiple scattering problem. We begin by considering the potential for the multiple scattering problem, $V(\mathbf{r}) = \sum_i v_i(\mathbf{r}_i - \mathbf{R}_i)$. In the following discussion, the muffin-tin approximation will be used, hence $v_i(\mathbf{r}_i - \mathbf{R}_i)$ is a set of single site muffin-tin potentials centred at $\mathbf{R}_i$. Muffin-tin potentials are spherically symmetric potentials within a certain radius and constant outside. It is also assumed that these potentials are non-overlapping (see Fig. 2.1).

In order to solve Eq. (2.21), one way is to introduce the scattering path operator,

$$\tau^{ij}(\epsilon) = v_i\delta_{ij} + \sum_k v_i G_0(\epsilon)\tau^{kj}(\epsilon). \tag{2.24}$$

This operator gives the scattered wave at the $j$th site when operated on an incident wave at the site $i$. From this, it can be shown that [27]

$$\tau^{ij}_{L,L'}(\epsilon) = t_{i,L}(\epsilon)\delta_{ij}\delta_{LL'} + \sum_{k\neq i}\sum_{L''} t_{i,L}(\epsilon)G_{0,LL'}(\mathbf{R}_i - \mathbf{R}_k;\epsilon)\tau^{kj}_{L'',L'}(\epsilon), \tag{2.25}$$

where $L$ and $L'$ are the angular momenta about sites $i$ and $j$ respectively, $t_i$ is the $T$-operator for the single-site potential $v_i$ and $G_{0,LL'}$ are known as the structure constants [28]. For a crystal of an element (i.e., pure metal), the $i$th and $j$th components of $\tau^{ij}_{L,L'}(\epsilon)$ will solely depend on the the vector distance $\mathbf{R}_i - \mathbf{R}_j$, since $t_L(\epsilon)$ will be the same on every site. Thus a lattice Fourier transform can be performed

on $\tau_{L,L'}$ and $G_{0,LL'}$, which are given by

$$\tau_{L,L'}(\mathbf{k};\epsilon) = \frac{1}{N}\sum_{ij}^{N} e^{-i\mathbf{k}.(\mathbf{R}_i-\mathbf{R}_j)}\tau^{ij}_{L,L'}(\epsilon) \tag{2.26}$$

and

$$G_{0,LL'}(\mathbf{k};\epsilon) = \frac{1}{N}\sum_{ij}^{N} e^{-i\mathbf{k}.(\mathbf{R}_i-\mathbf{R}_j)}G_{0,LL'}(\mathbf{R}_i-\mathbf{R}_j;\epsilon), \tag{2.27}$$

where $\mathbf{k}$ is restricted to the first Brillouin zone and $N$ is the total number of lattice sites. With these equations it follows that,

$$\tau_{L,L'}(\mathbf{k};\epsilon) = \left[\underline{t}^{-1}(\epsilon) - \underline{G}_0(\mathbf{k};\epsilon)\right]^{-1}, \tag{2.28}$$

where $\underline{G}_0(\mathbf{k};\epsilon)$ is the matrix $G_{0,LL'}(\mathbf{k};\epsilon)$ and $\underline{t}^{-1}(\epsilon)$ is a diagonal matrix with elements $t_L^{-1}(\epsilon)$.

Eq. (2.3) is very important in deriving what is known as the KKR secular equation which can be used to determine the band structure of a periodic crystal,

$$|| \; t_L^{-1}(\epsilon)\delta_{LL'} - G_{0,LL'}(\mathbf{k};\epsilon) \; || = 0. \tag{2.29}$$

This secular equation comes from the fact that the divergence of Eq. (2.28) will indicate the existence of a scattered wave even for stationary states.

Finally, the GF needs to be evaluated in order to complete the DFT self-consistency approach. It can be shown that the GF can be written as [29]

$$G(\mathbf{r},\mathbf{r}';\epsilon) = \sum_{LL'} Z^i_L(\mathbf{r}_i;\epsilon)\tau^{ij}_{L,L'}(\epsilon)Z^j_{L'}(\mathbf{r'}_j;\epsilon) - \delta_{ij}\sum_L Z^i_L(\mathbf{r}_<;\epsilon)J^i_L(\mathbf{r}_>;\epsilon), \tag{2.30}$$

where $Z^n_L$ and $J^n_L$ are respectively the regular and irregular solutions to the Schrödinger equation for the potential $v_n(\mathbf{r}_n)$ with an angular character $L = (l, m_l)$. $\mathbf{r}_>$ and $\mathbf{r}_<$ stand for the largest and the smallest of the vectors $\mathbf{r}$ and $\mathbf{r}'$, respectively. With this GF the electron density from Eq. (2.16) can be calculated, which in turn can be used to calculate the new effective potential. This cycle can be repeated until self-consistency is achieved.

## 2.3 Substitutional Disordered Alloys

In a pure metal, the potential described in the preceding section is rather simple, as the potential is the same at every atomic sites and therefore perfectly periodic. This

thesis, however, mainly deals with substitutional disordered alloys, where there are several types of scattering potential distributed randomly with probabilities proportional to their concentration amongst the lattice sites. This is called substitutional because the atoms occupy only the lattice sites. The potential for such system is much more complicated and much cunning is needed in order to advance this part of the computation.

One can follow some approximation scheme and construct a fictitious system which produces the average properties of the true physical system. This is heart of the effective medium approach. In the following discussions, the system will be simplified to having only two different atoms $A$ and $B$, and their potential is denoted by $v_A(\mathbf{r}-\mathbf{R}_i)$ and $v_B(\mathbf{r}-\mathbf{R}_i)$ respectively. This simplification is merely to avoid the algebra becoming too ponderous and can easily be generalised to having more than two types of scattering potential.

The simplest model to solve for such disordered alloy is known as the *rigid band model* [30]. This model neglects the difference between the two potentials and thus assumes $v_A(\mathbf{r}) = v_B(\mathbf{r})$. The only difference between the systems is the number of electrons per atom. This harsh treatment of the alloy may only be applicable to systems where the elements are immediate neighbours in the periodic table and carry the same crystal structure [31].

Another simple approach is the *virtual crystal approximation* (VCA). This approximation is more sophisticated than the rigid band model, as it includes the effect of the different of potentials in an average potential weighted by their concentrations (i.e., $v_{av}(\mathbf{r}) = cv_A(\mathbf{r}) + (1-c)v_B(\mathbf{r})$, where $c$ is the concentration for atom $A$). Although VCA has been recognised as an acceptable approximation for alloys, it still lack many physics associated with alloy systems and it is only reasonable for alloys with difference between $v_A(\mathbf{r})$ and $v_B(\mathbf{r})$ small [31].

A more superior model, which removed the limitations of both models described above, was later developed. It is a more abstract approach, which was taken by Soven [32], is to determine the effective medium self-consistently and is known as the *Coherent Potential Approximation* (CPA). It has been derived by extending the KKR method detailed in the previous section, thus the formalism is also called the KKR-CPA method [33, 34].

We will begin CPA by defining a coherent potential $v_c(\mathbf{r}-\mathbf{R}_i)$ to all lattice sites. For a site on the lattice, which we will call the central site, there will be a potential $v_\alpha(\mathbf{r}-\mathbf{R}_i)$, where $\alpha$ is either atom $A$ or $B$ (see Fig. 2.2). A conduction electron moving in this otherise periodic potential will therefore be scattered by the potential $v_\alpha$ when it reaches the central site. $A$ and $B$ are hence impurities and this

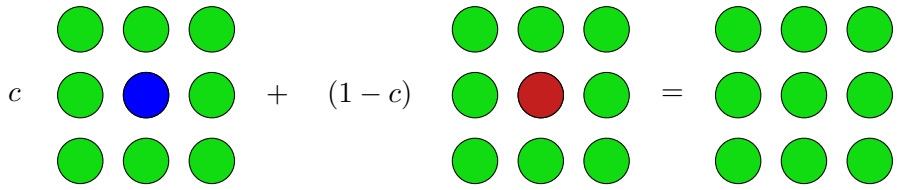


Figure 2.2: The construction of the coherent potential. The green circles represent an effective average potential and the blue and red atoms are atom $A$ and $B$ respectively. This equation indicates that the weighted average over sites $A$ and $B$ with concentration $c$ is needed to be the same as the average potential.

is equivalent to an impurity problem.

Since the choice of the impurity site is not important as the coherent potential lattice is translationally invariant, let us assume the impurity is at the 0th site. We will also define a single-site matrix $\widetilde{t}$, which describes scattering due to impurities in the pure coherent potential lattice and is given by

$$\widetilde{t}_{\alpha,0} = (v_{\alpha,0} - v_{c,0}) + (v_{\alpha,0} - v_{c,0}) G_c \widetilde{t}_{\alpha,0}, \tag{2.31}$$

at the 0th site and $G_c$ is the GF of the pure coherent potential lattice. The average of $\widetilde{t}_{\alpha,0}$ with respect to the occupation $\alpha$ is required to be zero, because by definition, $\widetilde{t}$ will be zero for sites of the effective medium. This means

$$c\widetilde{t}_{A,0} + (1-c)\widetilde{t}_{B,0} = 0. \tag{2.32}$$

From Eq. (2.22), the Dyson equation, $G_\alpha$ can be written in terms of the free-space GF $G_0$,

$$G_\alpha = G_0 + G_0 T_\alpha G_0, \tag{2.33}$$

where $T_\alpha$ is the total T-matrix for the system, which describes scattering by both the impurity potential $v_\alpha$ and the coherent potential $v_c$. Alternatively, $G_\alpha$ can be expressed in terms of the GF for the coherent potential lattice $G_c$,

$$G_\alpha = G_c + G_c T_{\alpha,0} G_c \tag{2.34}$$

and from Eq. (2.32), it follows that

$$G_c = cG_A + (1-c)G_B. \tag{2.35}$$

Substituting Eq. (2.33) into this equation will result in the total scattering matrix

for the pure coherent potential lattice $T_c$,

$$T_c = cT_A + (1-c)T_B, \tag{2.36}$$

which satisfies

$$G_c = G_0 + G_0 T_c G_0. \tag{2.37}$$

Eq. (2.36) gives the physical interpretation that on average, an impurity potential, when embedded into the effective medium, will cause no extra scattering. It is also generally used to define the KKR-CPA [35].

From the definition of our coherent potential, $v_c$ is the same on every sites. Without the impurity, the solution of the Eq. (2.25) is equivalent to that of a pure metal. So by taking the Fourier transform of Eq. (2.26) back to the real space will give

$$\tau^{00}_{c,L,L'}(\epsilon) = \frac{1}{\Omega_{BZ}} \int \left[\underline{t}_c^{-1}(\epsilon) - \underline{G}_0(\mathbf{k};\epsilon)\right]^{-1}_{L,L'} d\mathbf{k}, \tag{2.38}$$

where $\Omega_{BZ}$ is the volume of the Brillouin zone and $\underline{t}_c^{-1}(\epsilon)$ is a diagonal matrix with elements $t^{-1}_{c,L}(\epsilon)$. Note that $t_c$ is the single site t-matrix for the coherent potential $v_c$.

With the impurity, the scattering path operator, $\tau^{00}_{c,L,L'}$ will not be in the same simple form as Eq. (2.38) because now the scattering potentials are dependent on the site and the t-matrices are given by $t^i_L = t_{c,L} + (t_{\alpha,L} - t_{c,L})\delta_{i0}$. However, it is possible to express $\tau^{00}_{\alpha,L,L'}(\epsilon)$ in terms of $\tau^{00}_{c,L,L'}(\epsilon)$ by considering the full matrix form of the scattering path operators $\tau^{ij}_{c,L,L'}(\epsilon)$ and $\tau^{ij}_{c,L,L'}(\epsilon)$, which results in [36]

$$\tau^{00}_{\alpha,L,L'}(\epsilon) = \left[\tau^{00}_c \left(1 + (t_\alpha^{-1} - t_c^{-1})\tau^{00}_c\right)^{-1}\right]_{LL'}. \tag{2.39}$$

Now by using the CPA condition, Eq. (2.36) and identitifying that $T = \sum_{ij} \tau^{ij}$, a closed set of equations can be formed. It will arrive at

$$\tau^{00}_{c,L,L'}(\epsilon) = c\tau^{00}_{A,L,L'}(\epsilon) + (1-c)\tau^{00}_{B,L,L'}(\epsilon). \tag{2.40}$$

This is a self-consistency criterion for the multiple scattering substitutional alloy problem. This is almost enough to close the loop in the self-consistent calculations. The final quantities needed are the partially averaged charge densities, $\overline{n}_\alpha(\mathbf{r})$, for $\alpha$ being atom $A$ and $B$. $\overline{n}_\alpha(\mathbf{r})$ is defined formally by evaluating the charge density at a site, then averaging over all possible alloy configurations, with the constraint that the potential is always $v_\alpha$ at that specific site. Recall Eq. (2.16), the electron

density, this means that $n_\alpha(\mathbf{r})$ can be calculated with the GF appropriately averaged over all possible alloy configurations from Eq. (2.30). This can now close the loop from the effective potentials to the density and back, completing the self-consistent field KKR-CPA (SCF-KKR-CPA) scheme.

# Chapter 3

# Half-metals

## 3.1 Heusler alloys and properties of half-metals

Heusler alloys are intermetallic compounds which were first considered by Heusler in 1903 [37], although half-metallic behaviour of some of them was not discovered until 1983 by de Groot *et al* [4]. There are two families of Heusler alloys. First, the full Heusler alloys, which have the form $X_2YZ$, where $X$ and $Y$ are normally transition metals and $Z$ is typically an element from group IVB. They adopt the ordered $L2_1$-type structure, which consists of four interpenetrating face-centered-cubic (FCC) lattices (see Fig. 3.1a). Secondly, the half Heusler alloys, which were discovered after the full Heusler alloys, when it was found that it is possible to leave one of the four sublattices unoccupied and hence they have the form $XYZ$ and the $C1_b$ structure.

Full Heusler alloys do not just exist in $L2_1$ structure, they also exist in other structures, namely the partially disordered $B2$, the partially disordered $D03$ and the fully disordered $A2$ structures [38]. They still have the same FCC structure, but for $B2$, there is disordering between the $Y$ and $Z$ elements, meaning that the sublattice is randomly occupied by the $Y$ and $Z$ atoms. The $B2$ structure can therefore be constructed using the primitive cell or simple cubic (SC) (as shown in Fig. 3.1). For $D03$, it is similar to $B2$ but the disordering is between the $X$ and $Y$ elements. For $A2$, the disordering also occurs between $X$ and $YZ$ sublattices, hence fully disordered.

The simplest way to explain HMs is via the Kohn-sham electronic density of states (DOS). HM can be considered as the hybrid between metals and insulators or semiconductors. In normal metals, the DOS is non-zero at the Fermi level $\epsilon_f$, which allows electrons to be easily excited above $\epsilon_f$ or the conduction band, leading

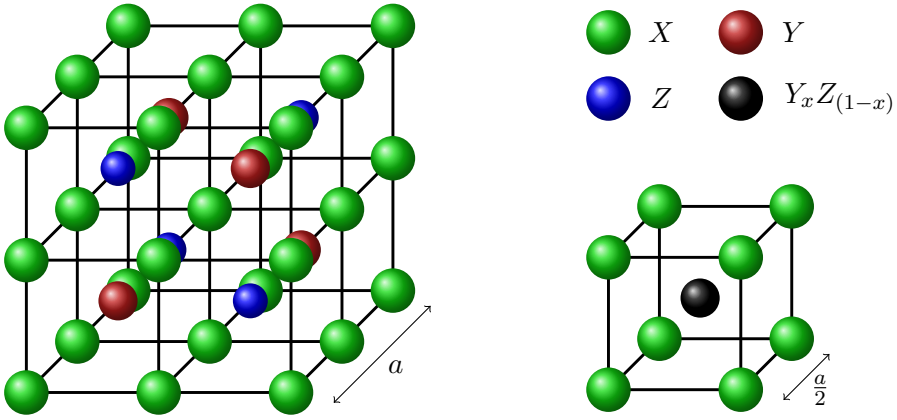


(a) (b)

Figure 3.1: Schematic view of (a) $L2_1$ structure. The lattice consists of 4 interpenetrating FCC sublattices. The unit cell is an FCC lattice with 4 atoms as the basis: $X_1$ $(0\,0\,0)$, $X_2$ $\left(\frac{1}{2}\,\frac{1}{2}\,\frac{1}{2}\right)$, $Y$ $\left(\frac{1}{4}\,\frac{1}{4}\,\frac{1}{4}\right)$ and $Z$ $\left(\frac{3}{4}\,\frac{3}{4}\,\frac{3}{4}\right)$. $a$ is the lattice parameter. (b) Simplified $B_2$ structure. This is a primitive cell or a SC as there are no distinctions between the $Y$ and $Z$ sites now, but replaced by a single $Y_xZ_{1-x}$ atom, where $x$ is the concentration of the $Y$ atom. The lattice parameter with respect to the $L2_1$ structure is $a/2$.

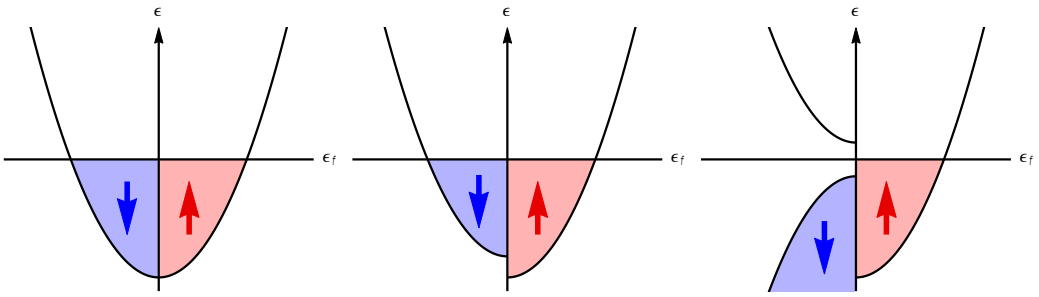


(a) Metals (b) Ferromagnets (c) Half-metals

Figure 3.2: Schematic representations of DOS for (a) metals, (b) ferromagnets and (c) half-metals. The shaded areas represent the occupied states at $T = 0$ and the arrows denote the spin orientation. Note that the horizontal line is where $\epsilon = \epsilon_f$.

to conduction, as shown in Fig. 3.2a. Insulators are very different as they possess a large band gap at $\epsilon_f$ stopping the electrons from being excited into the conduction band. HM acquire the behaviour of both of these materials since they possess the DOS of both metals and insulators in separate spin channels (see Fig. 3.2c).

An interesting property of Heusler alloys is that at $T = 0$, they possess integer spin magnetisation. In a stoichiometric compound (one that has a formula $X_aY_b$, where $a$ and $b$ are integers), the number of electrons per unit cell $N = N_\uparrow + N_\downarrow$ is an integer [39]. In a HM, the presence of a band gap at $\epsilon_f$ for one spin channel means that the last occupied spin up or down band is filled and therefore contains integer number of electrons. Hence, the spin magnetisation in the units of Bohr magneton $M = N_\uparrow - N_\downarrow$, must also be an integer. In addition, the spin magnetisation should follow the *Slater-Pauling behaviour*, where the spin magnetisation scales linearly with the number of valence electrons $Z$. For the half Heusler alloys, it follows the simple rule that $M = Z - 18$ and for the full Heusler alloys, it follows the so-called 'rule of 24': $M = Z - 24$ [40].

Another property is that HMs are ferromagnetic, since all HM are ferromagnetic. Hence they are also known as half metallic ferromagnets. However, note that it has also been predicted that HMs can also be antiferromagnetic [41]. For the scope of this thesis, this will not be discussed further. Ferromagnets are materials with spontaneous magnetisation or a non-zero spin polarisation, $P > 0$ [42]. Spin polarisation at energy $\epsilon$ is defined as [43]

$$P = \frac{n_\uparrow(\epsilon) - n_\downarrow(\epsilon)}{n_\uparrow(\epsilon) + n_\downarrow(\epsilon)}. \tag{3.1}$$

In order to take the account of different transport properties and for comparison with experimental results, it is often useful that $P$ is weighted by the Fermi velocity, $v_f$ (for ballistic transport) or $v_f^2$ (for diffusive transport) [44, 45]:

$$P = \frac{n_\uparrow(\epsilon_f)v_{f,\uparrow}^n - n_\downarrow(\epsilon_f)v_{f,\downarrow}^n}{n_\uparrow(\epsilon_f)v_{f,\uparrow}^n + n_\downarrow(\epsilon)v_{f,\downarrow}^n}. \tag{3.2}$$

In ferromagnetic materials, the DOS for one spin polarity is shifted respect to the opposite polarity, as shown in Fig. 3.2b. This causes the DOS at $\epsilon_f$ for one polarity to differ with respect to that of the opposite polarity and thus from Eq. (3.1), $P > 0$. Going back to the DOS for HM, Fig. 3.2c, there is a band gap for spin down at $\epsilon_f$, thus $n_\downarrow(\epsilon_f) = 0$, which again from Eq. (3.1) means $P = 1$ (i.e., 100% spin polarisation). This band gap emerges from the separation of the bonding and the anti-bonding states created by the interaction between the $d$ orbitals of the

higher-valence transition metal atom like Co or Ni and the lower-valence transition metal atom like Mn or Cr [7, 43].

Ferromagnetic materials do not always have spontaneous magnetisation, their magnetisation can be destroyed by thermal excitations. This happens at the so-called Curie temperature $T_C$, which differs between materials, when a ferromagnet is above this temperature, it will loses its magnetisation and becomes a paramagnet. The cobalt based full Heusler alloys of the form $Co_2YZ$ have high values of $T_C$, which are the type of Heusler alloys studied here. It is believed that by changing the electron number, more robust HMs could be found, since the electron number could affects the properties of the alloy such as the Fermi level and band gap.

## 3.2 HCP and FCC Cobalt

Before we investigate the Heusler alloys, a simple Co structure in hexagonal closed packed (HCP) and FCC phase were looked at to demonstrate ferromagnetism in terms of the DOS. The lattice parameters for the HCP structure were taken to be $a = b = 2.503$Å and $c = 4.0574$Å [46]. For the FCC phase, $a = 3.548$Å [47]. Since cobalt is ferromagnetic, we expect the DOS for the spins to be shifted with respect to each other, as illustrated in Fig. 3.2b. This is indeed the case, as shown in Fig. 3.3, both the HCP and FCC phases have their spin down DOS shifted to a higher energy to that of spin up. The magnetisation, $M$, per cobalt site was found to be $\sim 1.5\mu_B$ for both HCP and FCC. This means that both HCP and FCC are ferromagnetic. Although the FCC phase is the first phase transition of the stable HCP phase for Co at $T = 720$K [47], but cobalt has a much higher $T_C$ at 841K [48] hence its ferromagnetic behaviour persists after this phase transition.

## 3.3 $L2_1$ $Co_2MnSi$ and $B_2$ $CoMn_{0.5}Si_{0.5}$

In this section the standard $Co_2MnSi$ which is known to have a 100% spin polarisation [49] is studied for both $L2_1$ and $B2$ phases. The electronic structure calculations were performed using the Munich SPRKKR package [15, 16], which is based on the SCF-KKR-CPA scheme detailed in Chapter 2. The crystal potential was created in the framework of the LDA and the Vosko, Wilk and Nussair (VWN) formula [50] was used for the exchange-correlation functional. $10^{-5}$ Ry for the largest potential error and an angular momentum cutoff number $l_{\max} = 3$ were used on the self-consistent cycle. The imaginary part of the GF, $\delta$ was taken to be 0.0005Ry and the scalar relativistic approximation was used instead of a fully relativistic calculation, where

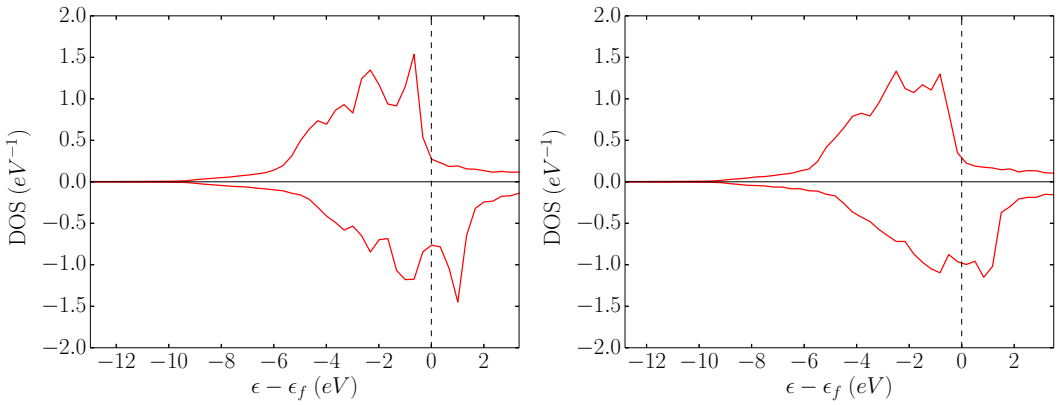


(a) HCP (b) FCC

Figure 3.3: Spin polarised DOS for Co, where (a) is the HCP structure and (b) is the FCC structure. Spin up and spin down are represented by positive and negative value of the DOS respectively. Both structures have similar DOS, in which the minority channel is shifted towards the conduction band with respect to the majority channel, thus demonstrating ferromagnetism.

the spin-orbit coupling effect is neglected [51]. These computational details were used across all the calculations.

The $L2_1$ $Co_2MnSi$ was constructed using the FCC structure (see Fig. 3.1a), with the lattice parameters $a = b = c = 5.645$Å [49]. The $B2$ $CoMn_{0.5}Si_{0.5}$ was constructed using the SC structure (see Fig. 3.1b), with the lattice parameters half of that of the $L2_1$ structure, $a = b = c = 2.823$Å. The DOS results from the calculations are shown in Fig. 3.4. Both structures clearly show a band gap only for the minority spin. However, the band gap seems to be situated just below the Fermi level, thus lowering the spin polarisation at the Fermi level. This is unexpected, since it is contradictory to the fact that $Co_2MnSi$ have a 100% spin polarisation and other published results [49, 52], in which alternative techniques were used. Though, it is believed that this shift of the Fermi level is a small numerical error.

The spin magnetisation per unit cell for $Co_2MnSi$ and $CoMn_{0.5}Si_{0.5}$ were calculated to be $5.1738\mu_B$ and $2.5493\mu_B$, respectively. Since the $B2$ phase has a unit volume half of the $L2_1$ phase, the spin magnetisation will also be halved. Hence for the same unit volume, the spin magnetisation for the $B2$ phase is $5.0986\mu_B$. Because the $L2_1$ phase contains 29 valence electrons, using the 'rule of 24' from the Slater-Pauling behaviour, one will arrive at the spin magnetisation of $5\mu_B$. This means that the calculations have overestimated the spin magnetisation. This problem is also related to the shift of the Fermi level, as it causes an increase of minority spin states at the Fermi level, therefore increasing the spin magnetisation.

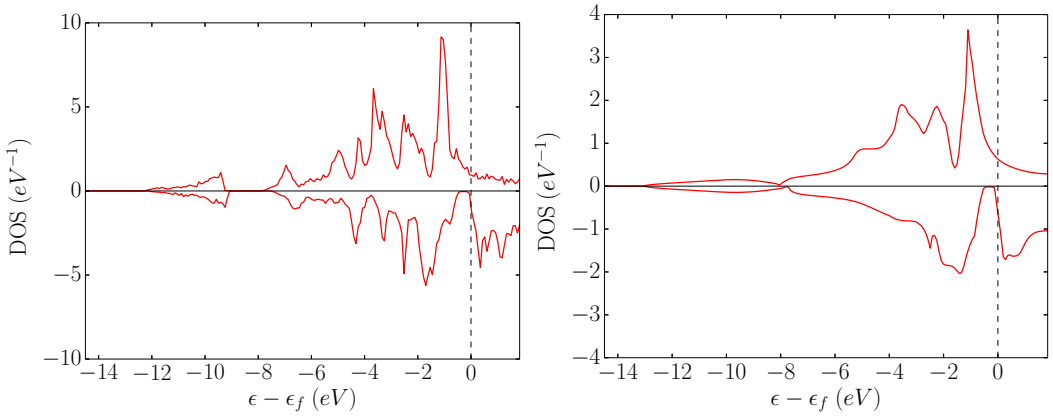


(a) $L2_1$ $Co_2MnSi$ (b) $B2$ $CoMn_{0.5}Si_{0.5}$

Figure 3.4: Spin polarised DOS for (a) $L2_1$ $Co_2MnSi$ and (b) $B2$ $CoMn_{0.5}Si_{0.5}$. Spin up and spin down are representated by positive and negative value of the DOS respectively.

Another point that can be seen is that the band gap is very small, about 0.4eV, compared with the size of 1eV which was calculated by others [49, 52, 53]. This is a well known problem, where the LDA would underestimate the band gap size by roughly 40% [54]. However, even with this underestimation, both structures is shown to be nearly half-metallic, and they become half-metallic with a small shift of the Fermi level. The underestimation of the band gap is not only from LDA but a general problem of DFT using standard functionals. A more sophisticated approach such as the many-body pertubation theory in GW-approximation (GWA) [55] could be used to fix semiconductor band gaps. However, this is not an important factor since this thesis is not looking to give exact calculations of the half-metallic properties but just the general trend on the effects of different compositions.

In summary, we have presented the properties of HMs and Heusler alloys, and how the half-metallicity of materials can be analysed through their DOS. In the next chapter, using the same SCF-KKR-CPA scheme, we will begin the analysis of a 5-components alloy, namely $CoFe_xMn_{0.5-x}Ga_ySi_{0.5-y}$, in the light of discovering new potential HMs. Attempts to counteract the problems described in this section and to extract trends from our results will also be presented.

# Chapter 4

# Half-metallicity of $\mathbf{CoFe}_x\mathbf{Mn}_{0.5-x}\mathbf{Ga}_y\mathbf{Si}_{0.5-y}$

To achieve the desired HM behaviour, it is necessary to investigate how different concentrations of different elements affect the half-metallicity of the alloy. Here, a 5-components alloy of the form $CoFe_xMn_{0.5-x}Ga_ySi_{0.5-y}$ was constructed, where $x$ and $y$ are the concentrations going from 0 to 0.5 for a $B2$ structure. The alloy was constructed using the SC structure, hence why the concentrations only go up to 0.5. For simplicity, the lattice parameter $a = 2.823$Å was used for all the concentrations. 441 DOS data were simulated, using the computational details specified in previous section, with different permutations of the concentrations. In order to analyse these data, algorithms were designed to study the criteria required for HM behaviour. Due to the errors from the LDA, the algorithms were designed to only look for the trend from the effect of compositional disorder.

## 4.1 Band gap analysis

One of the criteria is to have a band gap at the Fermi level $\epsilon_f$ for the minority spin channel. As discussed in the previous section that there is a reduction of the band gap introduced by the LDA calculation. This means that one can not simply calculate the band gap size because it is not accurate and the reduction can cause the band gap to close up completely. But we can use the LDA calculations to extract half-metallic trends. The band gap was studied by integration, which calculates the number of states in the vicinity of $\epsilon_f$. If the alloy does indeed have a band gap, then the integral should be near or equals to zero. Conversely, if the alloy does not have a band gap, then the integral will be far from zero.

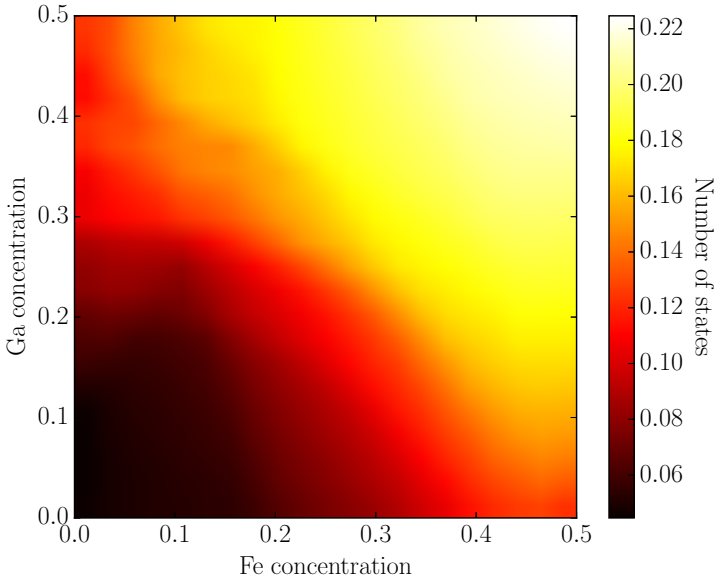


Figure 4.1: Band gap analysis for minority spin. The darker and lighter region correspond to alloys with and without a band gap, respectively. Here, the darker region is the region of interest.

Individual minority spin DOS data were first linearly interpolated to allow for better integration, but because of the small error in pinpointing $\epsilon_f$, an integration cannot be performed directly around $\epsilon_f$, as the band gap might not be exactly there. A more sophisticated approach was designed, where the band gap integral is

$$I_{\text{bg}} = \min \left\{ \int_{a+\delta}^{a+k+\delta} n(\epsilon) d\epsilon \;\middle|\; \delta \in (0, -a) \right\}. \tag{4.1}$$

This equation select the correct band gap integral by integrating a fixed width strip with size $k$, translating this strip and perform the integral again, repeat this until $a + \delta = 0$, then take the smallest integral value. The values $a = -0.5$eV and strip size $k = 0.4$eV, where the translation step size is $+0.05$eV, were used to produce the results shown in Fig. 4.1. These parameters were chosen on the basis of the lowest value that the valence band maximum can take is about $-0.5$eV and the largest band gap size is about 0.4eV. Note that if $k$ is set much smaller than the largest band gap then larger area of the result would present itself as having a large band gap. For example, if $k = 0.2$eV then any band gap more than 0.2eV will have roughly the same integral.

Fig. 4.1 shows that the lower the concentration of Fe and Ga, the bigger the band gap. This becomes apparent when taking the DOS from the two opposite

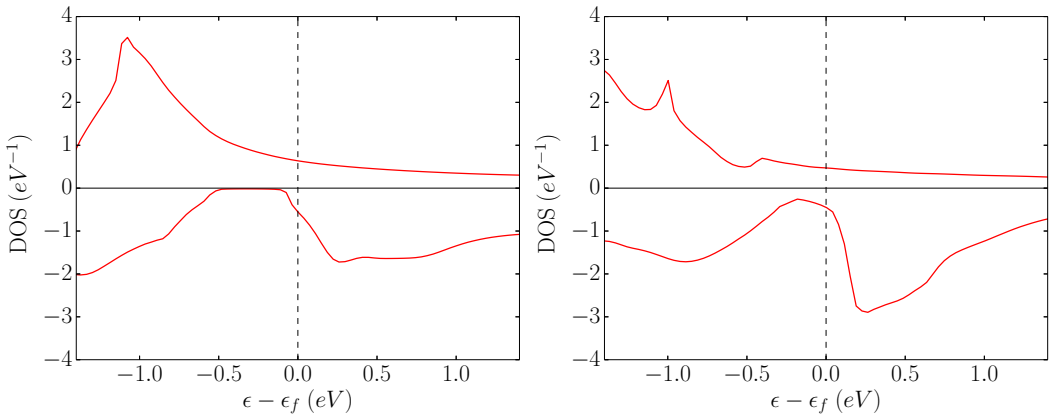


(a) $CoFe_0Mn_{0.5}Ga_{0.025}Si_{0.475}$ (b) $CoFe_{0.5}Mn_0Ga_{0.5}Si_0$

Figure 4.2: Spin polarised DOS plot of (a) $CoFe_0Mn_{0.5}Ga_{0.025}Si_{0.475}$, where there is a big band gap, and (b) $CoFe_{0.5}Mn_0Ga_{0.5}Si_0$, where there is no band gap.

ends of the graph, as shown in Fig. 4.2. Both Fe and Ga have more electrons than Mn and Si, respectively, so having higher concentration of them means adding more electrons. From Fig. 4.2, it seems to suggest that adding more electrons will fill more states near $\epsilon_f$, which causes the band gap to close up. It can also be seen from Fig. 4.1, that the increase of Fe has a greater impact on the band gap than the increase of Ga. This can be explained from the fact that the origin of the band gap is from the interactions between the higher-valence transition metal atom, in this case the Co, and the lower-valence transition metal atom, in this case the Fe and the Mn. This means that Fe would play a more important role than Ga for the induction of the band gap.

## 4.2 Density of states difference at Fermi energy

Another important criterion is the difference in DOS between spin up and down at $\epsilon_f$. This allows us to gain insights into the magnetisation and polarisation at $\epsilon_f$. Again, due the numerical error in locating $\epsilon_f$, it is not possible to take the difference directly. A simplified approach was used to correct $\epsilon_f$, where the new $\epsilon_f$ is estimated by finding the lowest value of $n^{\downarrow}_{\text{tot}}$ in the vicinity of the original $\epsilon_f$. Then the difference is simply calculated by

$$I_{\text{DOS}} = n^{\uparrow}_{\text{tot}}(\epsilon_f) - n^{\downarrow}_{\text{tot}}(\epsilon_f). \tag{4.2}$$

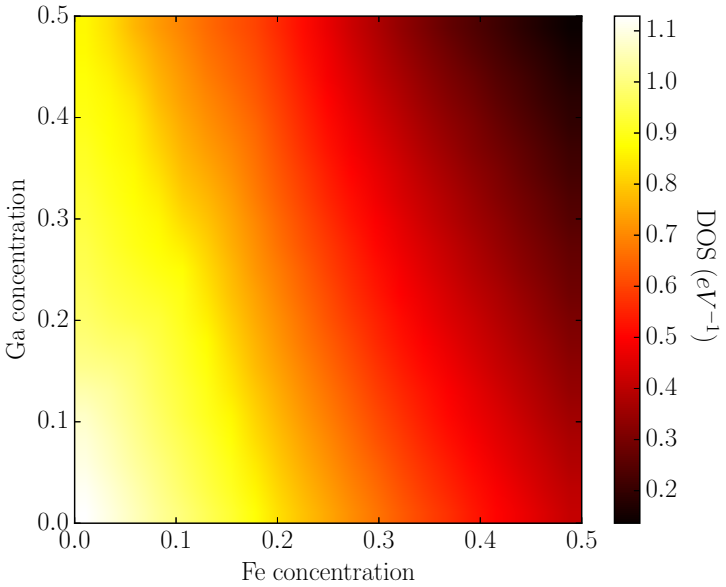


Figure 4.3: DOS difference analysis. The ligher and darker region correspond to alloys with high and low DOS difference, respectively. Here, the lighter region is the region of interest.

The range of $(\epsilon_f - 0.5)$ eV and $(\epsilon_f + 0.5)$ eV was used to look for the new $\epsilon_f$. The results from this calculation is shown in Fig. 4.3. It shows a similar relation to the band gap analysis (see Fig. 4.1), where having high concentration of both Fe and Ga is not ideal, and that there is a greater freedom towards increasing the Ga concentration. The band gap tends to vanish on the increase of the Fe and the Ga concentrations, which raises the minority DOS, thus decreasing the DOS difference. However, there is a possibility that the LDA can cause the band gap to close up even if the alloy does indeed have a band gap. One cannot also assume that all the alloys have a band gap and therefore just look at the correlation between the concentrations and the majority DOS. This is certainly a limitation of using the LDA. Nevertheless, for illustration of the general trend between the concentrations and the DOS difference, this is enough.

## 4.3 Potential half-metals from density of states analysis

With these 2 criteria established, we can combine the values calculated to find the best candidates for the potential HM. However, if the values are summed together as they are, it will impose a problem with the weighting. For example, Fig. 4.3 and Fig. 4.1 show that the DOS difference calculations will be weighted more heavily

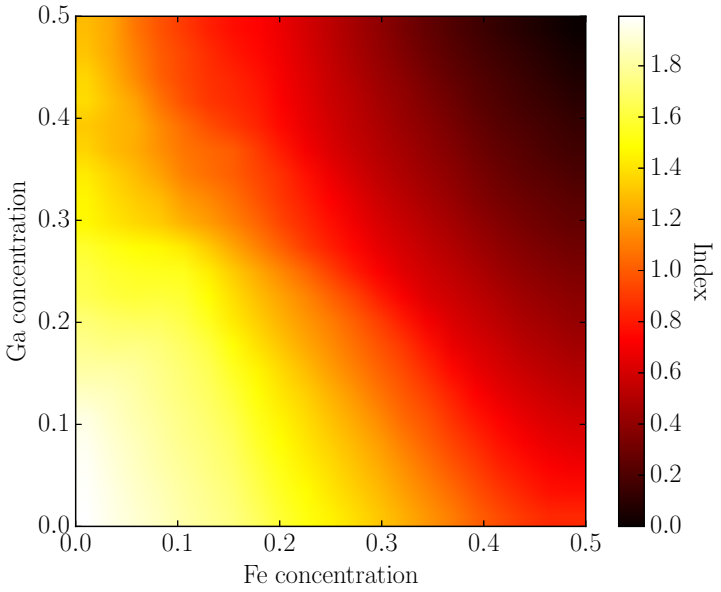


Figure 4.4: Combination of the band gap and DOS difference at $\epsilon_f$, where higher index shows alloys with behaviour closest to or is HM. The lighter region where the Ga and Fe concentration are low is therefore the region of interest.

than the band gap calculations when summed (i.e., DOS difference is taken to be more important than the band gap). To resolve this issue, each of the analyses were rescaled to 0 to 1 before summing, assuming that each one is weighted the same. They were rescaled via

$$I_{\text{rescaled}} = \frac{I - I_{\text{min}}}{I_{\text{max}} - I_{\text{min}}}, \tag{4.3}$$

where $I_{\text{max}}$ and $I_{\text{min}}$ are the largest and smallest value of the analysis, respectively.

In the following discussion, $I$ will be referred to as the *index*. This index is defined as a measure how close a material is to a HM, where the larger the index, the closer it is to a HM. Note that for the band gap analysis, the calculated values had to be inverted (i.e., $1 - I_{\text{bg}}$) before rescaling, because the smallest value represents the material closest to a HM and the largest value represents the material furthest from a HM. With the indices rescaled and summed, it will result in Fig. 4.4.

Fig. 4.4 indicates that the best candidates for potential HMs are in the region where there are low concentrations of Ga and Fe. Moreoever, the half-metallicity seems to be more sensitive to the increase of Fe than the increase of Ga. This is just an initial conclusion, it is necessary to look at the transport properties at $\epsilon_f$ to further support this conclusion, which is presented in the next chapter.

# Chapter 5

# Transport Properties of Solids

The previous chapter has discussed different methods of analysing the DOS to determine the best candidates for HM. However, the methods were all based on analysing the magnetic behaviour of the material and have missed out an important factor, the electrical conductivity. This chapter will begin by describing the basic theory behind electrical conductivity, followed by a more refined theory. Then how the transport properties can be analysed through the Bloch spectral function (BSF) is presented. Finally, we then continue the investigation into the $CoFe_xMn_{0.5-x}Ga_ySi_{0.5-y}$ alloy from Chapter 4.

## 5.1 Drude model

An early attempt to explain the existence of currents through metals was made by Weber in 1875 [1]. His idea was that a molecule of a metal consisted of a positive charged particle orbiting around a negative charged particle and upon application of an external electromotive force, the orbital radius would increase until the positive charge leaves the molecule and captured by another molecule. This will then continue through the metal while the electromotive force is active, thus achieving a current. The theory of electrical conduction was better understood after the discovery of electrons by J. J. Thomson in 1897 [56].

The first theoretical model of electrical conduction is the *Drude model* proposed by Drude in 1900 [57], which is an application of kinetic theory. In the following discussion, let us assume the metal is isotropic. The model assumes that there are free electrons in a metal forming an *ideal gas* (i.e., non-interacting point particles that pursue random motions) and have an average velocity $\langle \mathbf{v} \rangle$. The elec-

trical conductivity $\sigma$, from the macroscopic viewpoint is defined by Ohm's law [58]

$$\mathbf{J} = \sigma \mathbf{E}, \tag{5.1}$$

where $\mathbf{J}$ is the current density resulting from an applied electric field $\mathbf{E}$. From the microscopic point of view, the current density is given by

$$\mathbf{J} = -ne\langle \mathbf{v} \rangle, \tag{5.2}$$

where $n$ is the electron density and $-e$ is the electron charge.

Suppose now that during some time interval $dt$, there is a probability $dt/\tau$ for an electron to collide with an ion, where $\tau$, for simplicity, is assumed to be a constant. We will also assume that during the collision, the electron loses all its energy gained from the electric field and its velocity is random after the collision. Under these assumptions, the rate of change of $\langle \mathbf{v} \rangle$ due to the field alone and due to collisions alone are

$$\left( \frac{\partial \langle \mathbf{v} \rangle}{\partial t} \right)_{\text{field}} = -\frac{e\mathbf{E}}{m} \quad \text{and} \quad \left( \frac{\partial \langle \mathbf{v} \rangle}{\partial t} \right)_{\text{coll}} = -\frac{\langle \mathbf{v} \rangle}{\tau}, \tag{5.3}$$

respectively. Hence, the following must be satisfied for a steady state,

$$\frac{d\langle \mathbf{v} \rangle}{dt} = \left( \frac{\partial \langle \mathbf{v} \rangle}{\partial t} \right)_{\text{field}} + \left( \frac{\partial \langle \mathbf{v} \rangle}{\partial t} \right)_{\text{coll}} = 0. \tag{5.4}$$

From this, it follows directly that the average velocity is given by

$$\langle \mathbf{v} \rangle = \left( -\frac{e\tau}{m} \right) \mathbf{E}. \tag{5.5}$$

This average velocity due to an electric field is also known as *drift velocity*. It can be shown from Eq. (5.2) and Eq. (5.5) that the conductivity is given by

$$\sigma = ne^2\tau/m. \tag{5.6}$$

This equation form the basis of Drude model for electrical conductivity.

Going back to the rate of change of the drift velocity due to collisions alone, Eq. (5.3), the solution is

$$\langle \mathbf{v}(t) \rangle = \langle \mathbf{v}(0) \rangle e^{-t/\tau}. \tag{5.7}$$

The physical meaning of this equation is that if an electric field is suddenly switched off at $t = 0$, where the electrons at that time have a drift velocity of $\langle \mathbf{v}(0) \rangle$, the

drift velocity will gradually approach zero. This means that $\tau$ is the *relaxation time*, because of the exponential nature of Eq. (5.7).

In our case where the velocity after collision is random, the relaxation time can also be considered to be the *mean free time* of the collisions or the *lifetime* of the electrons. This will be shown as follows. Let $P(t)$ and $P(t+dt)$ be the probability that an electron has not collided again after $t$ and $t+dt$ seconds, respectively, after a collision has occurred. One can write

$$P(t+dt) = P(t) + (dP/dt)dt \tag{5.8}$$

and may also write

$$P(t+dt) = P(t)P(dt) = P(t)(1 - dt/\tau), \tag{5.9}$$

where $1 - dt/\tau$ represents the probability for an electron not to collide during the interval $dt$. From the last two equations and the fact that $P = 1$ for $t = 0$, it follows that

$$P(t) = e^{-t/\tau}. \tag{5.10}$$

Hence the mean free time between collisions is

$$\langle t \rangle = \int_0^\infty t(dP/dt)dt = \tau. \tag{5.11}$$

It must be emphasized that this definition of the mean free time, that it is identical to the relaxation time, is only true if the velocity after collision is random. If the scattering is not isotropic, the relaxation time can easily be shown to be

$$\tau = \tau_c/(1 - \langle \cos\beta \rangle), \tag{5.12}$$

where $\tau_c$ is the mean free time between collisions and $\langle \cos\beta \rangle$ is the average of the cosine of the scattering angle.

The drastic assumption that the electrons form an ideal gas is a very crude treatment, as they are now known to follow the Fermi-Dirac distribution and have noticeable interactions. However, we shall see later that by using a more sophisticated method, for certain cases, it can be well modelled by Drude model.

## 5.2 Boltzmann transport equation

The usage of average properties such as the average velocity and the relaxation time solely, as used by the Drude model, is rarely possible in strict analysis of transport phenomena. It is more instructive to look at the spatial coordinates of the electrons and how many are travelling to the left and right with a certain velocity. Therefore it is necessary to determine a distribution function for the electrons for a given external field.

For simplicity, the following discussion will only be in 1 dimension. Let us assume there exists a distribution function $f(r_x, p_x; t)$ that determines the probability that a state is occupied at some particular position $r_x$, momentum $p_x$ and time $t$. For ballistic transport, where scattering does not occur, it will follow *Liouville's theorem* [59] that along any trajectory in phase space, the distribution function is invariant, i.e., $df/dt = 0$. The total derivative is thus

$$\frac{df}{dt} = \frac{\partial f}{\partial t} + \frac{\partial f}{\partial r_x}\frac{dr_x}{dt} + \frac{\partial f}{\partial p_x}\frac{dp_x}{dt} = \frac{\partial f}{\partial t} + \frac{\partial f}{\partial r_x}v_x + \frac{\partial f}{\partial p_x}F_x = 0, \tag{5.13}$$

where $F_x = \frac{dp_x}{dt}$, the force in the x-direction. This can be generalised to 3 dimensions and writing $\mathbf{p} = \hbar\mathbf{k}$, giving

$$\frac{\partial f}{\partial t} + \mathbf{v} \cdot \nabla_{\mathbf{r}} f + \mathbf{F} \cdot \nabla_{\mathbf{k}} f = 0. \tag{5.14}$$

In the presence of scattering, there will be electrons scattering into and out of a certain state, which would change the probability of that state being occupied. Hence, the zero from Eq. (5.14) would be replaced by some net rate of change of states. If we let $[\partial f/\partial t]_{\text{scatt}}$ be this rate of change, then we can write

$$\frac{\partial f}{\partial t} + \mathbf{v} \cdot \nabla_{\mathbf{r}} f + \mathbf{F} \cdot \nabla_{\mathbf{k}} f = \left[\frac{\partial f}{\partial t}\right]_{\text{scatt}}. \tag{5.15}$$

For a steady state $\partial f/\partial t = 0$. The force $\mathbf{F}$ is from the effect of the external electric $\mathbf{E}$ and magnetic fields $\mathbf{H}$ and is defined as

$$\mathbf{F} = -\frac{e}{\hbar}\left(\mathbf{E} + \frac{1}{c}\mathbf{v} \times \mathbf{H}\right). \tag{5.16}$$

This will result in

$$\mathbf{v} \cdot \nabla_{\mathbf{r}} f - \frac{e}{\hbar}\left(\mathbf{E} + \frac{1}{c}\mathbf{v} \times \mathbf{H}\right) \cdot \nabla_{\mathbf{k}} f = \left[\frac{\partial f}{\partial t}\right]_{\text{scatt}}, \tag{5.17}$$

which is the *Boltzmann transport equation* in its general form [2].

The scattering term is what makes the Boltzmann equation difficult. In order to find an expression for this scattering, suppose that $\mathscr{W}(\mathbf{k}, \mathbf{k}')$ is the intrinsic probability that an electron makes a transition from the state $\mathbf{k}$ to state $\mathbf{k}'$. To include the effect of the exclusion principle, we must multiply $\mathscr{W}(\mathbf{k}, \mathbf{k}')$ with $f(\mathbf{k})$, the chance of an electron being occupied in the initial state $\mathbf{k}$, and $1 - f(\mathbf{k}')$, the chance for the final state $\mathbf{k}'$ being vacant initially. Hence, the probability of a transition into $\mathbf{k}'$, if $\mathbf{k}'$ lies in the range of $d\mathbf{k}'$ is

$$\mathscr{P}(\mathbf{k}, \mathbf{k}')d\mathbf{k}' = f(\mathbf{k})\Big\{1 - f(\mathbf{k}')\Big\}\mathscr{W}(\mathbf{k}, \mathbf{k}')d\mathbf{k}'. \tag{5.18}$$

A similar relation can be written for the transition from $\mathbf{k}'$ to $\mathbf{k}$,

$$\mathscr{P}(\mathbf{k}', \mathbf{k})d\mathbf{k}' = f(\mathbf{k}')\Big\{1 - f(\mathbf{k})\Big\}\mathscr{W}(\mathbf{k}', \mathbf{k})d\mathbf{k}'. \tag{5.19}$$

The net change in $f$ is simply the difference between these two expressions and sum over all the states $\mathbf{k}'$, that is,

$$\left[\frac{\partial f}{\partial t}\right]_{\text{scatt}} = \int \Big[\mathscr{W}(\mathbf{k}', \mathbf{k})f(\mathbf{k}')\big\{1 - f(\mathbf{k})\big\} - \mathscr{W}(\mathbf{k}, \mathbf{k}')f(\mathbf{k})\big\{1 - f(\mathbf{k}')\big\}\Big]d\mathbf{k}'. \tag{5.20}$$

In equilibrium, we can write $f$ as the Fermi-Dirac distribution function $f_0$ and Eq. (5.20) must vanish, thus we can define a function $W(\mathbf{k}, \mathbf{k}')$ to be

$$W(\mathbf{k}, \mathbf{k}') = e^{E_{\mathbf{k}'}/kT}\mathscr{W}(\mathbf{k}, \mathbf{k}') = e^{E_{\mathbf{k}}/kT}\mathscr{W}(\mathbf{k}', \mathbf{k}). \tag{5.21}$$

If we assume that when a current is present, the transition probabilities are the same as that of in equilibrium state. Then, it will result in

$$\begin{aligned}\left[\frac{\partial f}{\partial t}\right]_{\text{scatt}} = \int W(\mathbf{k}, \mathbf{k}')\Big[ & e^{-E_{\mathbf{k}}/kT}f(\mathbf{k}')\big\{1 - f(\mathbf{k})\big\} \\ & - e^{-E_{\mathbf{k}'}/kT}f(\mathbf{k})\big\{1 - f(\mathbf{k}')\big\}\Big]d\mathbf{k}'.\end{aligned} \tag{5.22}$$

When $\mathscr{W}(\mathbf{k}, \mathbf{k}')$ is known, the formal theory of electrical conductivity is involved with the solution of Eq. (5.17) and Eq. (5.22).

In order to get an idea of the form of the conductivity, we will again assume there exists a time relaxation, as described in the preceding section, so that

$[\partial f/\partial t]_{\text{scatt}}$ takes the form

$$\left[\frac{\partial f}{\partial t}\right]_{\text{scatt}} = -\frac{(f - f_0)}{\tau}. \tag{5.23}$$

Furthermore, we will assume $H = 0$, $\nabla_r f = 0$ and can neglect terms in $\mathbf{E}^2$, because the electric field is always small in a metal. Writing $f = f_0$ from Eq. (5.17) and the above definition of the time relaxation will result in

$$f = f_0 + \frac{e}{\hbar}\tau \mathbf{E} \cdot \nabla_{\mathbf{k}} f_0 = f_0 + e\tau \mathbf{v} \cdot \mathbf{E}\frac{\partial f_0}{\partial \epsilon}. \tag{5.24}$$

With this, we can calculate the current density using

$$\mathbf{J} = -\frac{e}{4\pi^3}\int \mathbf{v} f d\mathbf{k} = -\frac{e^2}{4\pi^3}\int \tau \mathbf{v}(\mathbf{v} \cdot \mathbf{E})\frac{\partial f_0}{\partial \epsilon} d\mathbf{k}. \tag{5.25}$$

From Ohm's law, Eq. (5.1), the conductivity tensor is therefore

$$\underline{\sigma} = -\frac{e^2}{4\pi^3}\int \tau \mathbf{v}\mathbf{v}\frac{\partial f_0}{\partial \epsilon} d\mathbf{k}. \tag{5.26}$$

This is a tensor, meaning that the conductivity can be different for different directions (i.e., an anisotropic material).

The integral from Eq. (5.26) can be evaluated by considering the $\mathbf{k}$-space to be divided up by the set of surfaces $\epsilon(\mathbf{k}) =$ constant. If $d\mathbf{k}$ is an element contained between the surfaces $\epsilon$ and $\epsilon + d\epsilon$, then

$$d\mathbf{k} = dS d\epsilon/(d\epsilon/dn), \tag{5.27}$$

where $dS$ is an element of surface and $d\epsilon/dn$ is the normal derivative of $\epsilon$, which is also $d\epsilon/dn = |\nabla_{\mathbf{k}}\epsilon|$, and thus

$$\underline{\sigma} = -\frac{e^2}{4\pi^3}\int \frac{\partial f_0}{\partial \epsilon} d\epsilon \int \frac{\tau \mathbf{v}\mathbf{v}}{|\nabla_{\mathbf{k}}\epsilon|} dS, \tag{5.28}$$

where the first integral with respect to $\epsilon$ can be calculated by the use of the asymptotic formula to any order [2],

$$-\int_0^\infty \phi(\epsilon)\frac{\partial f_0}{\partial \epsilon} d\epsilon = \phi(\epsilon_f) + 2\sum_{n=1}^{\infty} c_{2n}(kT)^{2n}\frac{d^{2n}\phi(\epsilon_f)}{d\epsilon_f^{2n}}, \tag{5.29}$$

where $c_{2n} = \sum_{s=1}^{\infty}[(-1)^{s+1}/s^{2n}]$. The first order approximation is

$$\underline{\sigma} = -\frac{e^2}{4\pi^3}\int_{\epsilon=\epsilon_f}\frac{\tau \mathbf{v}\mathbf{v}}{|\nabla_{\mathbf{k}}\epsilon|}dS. \tag{5.30}$$

With the conductivity in this form, it can be seen that by finding the relaxation time and the velocity of the electrons at the Fermi surface, the conductivity can be found. Another useful quantity that we could consider is the *mean free path* of the electrons, the average distance it travels between collisions, which is simply

$$\Lambda = \tau v. \tag{5.31}$$

Under isotropic conditions, the conductivity tensor becomes a scalar and would arrive back at the Drude model, Eq. (5.6).

## 5.3 Bloch spectral function

To look at the transport properties of the alloy, we turned to the Fermi surface. For defining this surface, a useful tool is the Bloch Spectral Function (BSF), which is related to the Fourier transformed averaged GF for the electrons [15, 60, 61], given by

$$A_B(\mathbf{k};\epsilon) = -\frac{1}{\pi N}\sum_{i,j}^{N} e^{i\mathbf{k}(\mathbf{R}_i-\mathbf{R}_j)}\,\mathrm{Im\,Tr}\int_{\Omega}\langle G(\mathbf{r}+\mathbf{R}_i,\mathbf{r}+\mathbf{R}_j;\epsilon)\rangle d\mathbf{r}, \tag{5.32}$$

where $i, j$ are lattice site indices and the integration is over the unit cell volume at the origin. From this expression, one can be seen as a $\mathbf{k}$-resolved DOS function,

$$n(\epsilon) = \frac{1}{\Omega_{BZ}}\int A_B(\mathbf{k};\epsilon)d\mathbf{k}, \tag{5.33}$$

because the imaginary part of the GF is associated to the DOS [60]. Within the KKR-CPA formalism, $A_B(\mathbf{k},\epsilon)$ is given as [29]

$$A_B(\mathbf{k};\epsilon) = -\frac{1}{\pi}\mathrm{Im\,Tr}\Big[\underline{F}_c\tau_{\mathrm{CPA}}(\mathbf{k};\epsilon)\Big] - \frac{1}{\pi}\mathrm{Im\,Tr}\Big[(\underline{F}_c - \underline{F}_{cc})\tau^{ii}_{\mathrm{CPA}}\Big], \tag{5.34}$$

where the matrices $\underline{F}_c$ and $\underline{F}_{cc}$ are defined in terms of the overlap integrals [60]

$$F_{L,L',\alpha\beta} = \int_{\Omega} Z_{L,\alpha*}(\mathbf{r};\epsilon)Z_{L',\beta*}(\mathbf{r};\epsilon)d\mathbf{r} \tag{5.35}$$

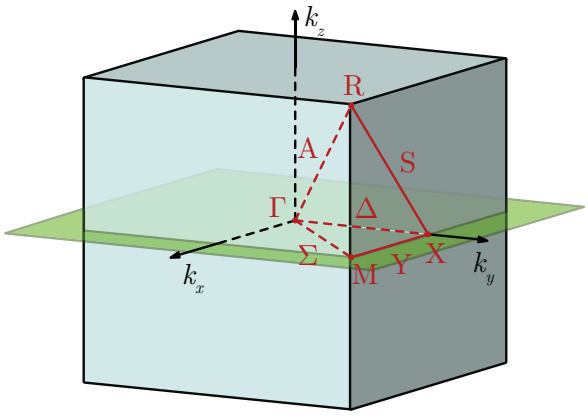


Figure 5.1: Brillouin zone for a primitive cell or a simple cubic lattice showing labels for special symmetry points. Cartesian coordinates of the symmetry points in units of $2\pi/a$ are $\Gamma = \left(0\,0\,0\right)$, $M = \left(0\,\frac{1}{2}\,0\right)$, $M = \left(\frac{1}{2}\,\frac{1}{2}\,0\right)$ and $M = \left(\frac{1}{2}\,\frac{1}{2}\,\frac{1}{2}\right)$. The green plane shows a slice of the cell spanned by the vectors $k_1 = (1\,0\,0)$ and $k_2 = (0\,1\,0)$, also known as the Γ-X×Γ-X plane.

and the matrices $\underline{\tau}_{\mathrm{CPA}}(\mathbf{k};\epsilon)$ and $\tau^{ii}_{\mathrm{CPA}}$ are analogous to Eq. (2.38).

For ordered systems (i.e., perfect crystal), the BSF is a set of $\delta$-functions,

$$A_B(\mathbf{k};\epsilon) = \sum_n \delta(\epsilon - \epsilon_n(\mathbf{k})), \tag{5.36}$$

where $n$ is the band index and $\epsilon_n(\mathbf{k})$ is the Bloch energy eigenvalue, which bears the same information as the usual dispersion relation. By fixing $\epsilon$ and going through $\mathbf{k}$, we will pick up some $\delta$ peaks at the energy eigenvalues. Repeating this for other $\epsilon$ values and picking up more $\delta$ peaks, the complete band structure picture would be found. The BSF is therefore an alternative way of representing the band structure with broadening according to the imaginary part of $\epsilon$. As an example, the BSF of the ordered $L2_1$ $Co_2MnSi$ is shown in Fig. 5.2a with the band structure well defined by the peaks of the BSF with small broadening.

For disordered systems, the more electron scattering by impurities, the wider the BSF [62]. With this broadening, the band structure is defined by the position of the peaks of the BSF. To demonstrate this, Fig. 5.2b shows the BSF of the $B2$ $CoMn_{0.5}Si_{0.5}$, where the peaks are very wide from the disordering, in contrast with the $L2_1$ $Co_2MnSi$ shown in Fig. 5.2a. However, the position of the peaks can still be interpreted as the band structure. If the effect of the disordering is somewhat

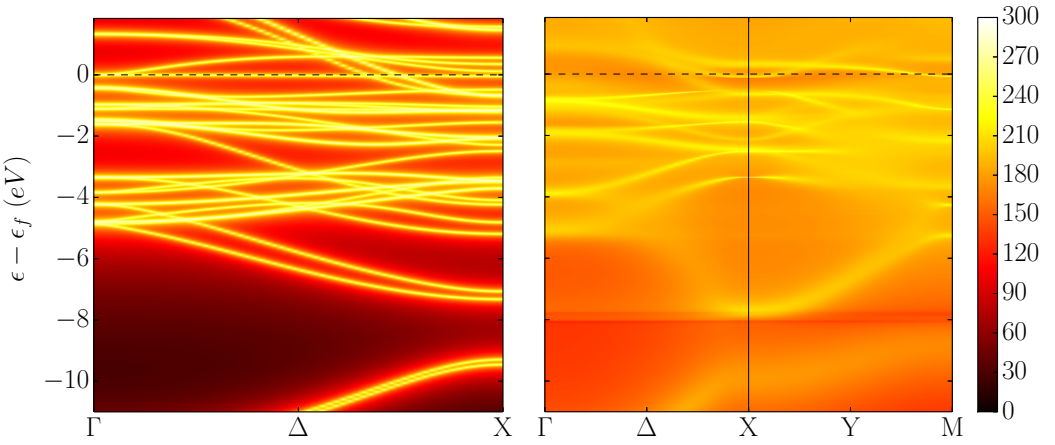


(a) $L2_1$ $Co_2MnSi$ (b) $B2$ $CoMn_{0.5}Si_{0.5}$

Figure 5.2: BSF of (a) $L2_1$ $Co_2MnSi$ from an FCC lattice along the path Γ-Δ-X and (b) $B2$ $CoMn_{0.5}Si_{0.5}$ from a primitive cell lattice along the path Γ-Δ-X-Y-M. The symmetry points and lines of a primitive cell are indicated the same as in Fig. 5.1. Both (a) and (b) used $\delta = 0.001$.

weak or moderate, it can be considered that it takes the form of a Lorentizian,

$$f(x; x_0, \Gamma, I) = I\left[\frac{\Gamma^2}{(x - x_0)^2 + \Gamma^2}\right], \tag{5.37}$$

where $x_0$ is the position of the peak, $I$ is the value at $x_0$ and Γ is the full width at half maximum (FWHM). For a fixed $k$ wavevector, Γ would be in energy and it is interpreted as an inverse lifetime [63],

$$\tau = \frac{\hbar}{\Gamma}. \tag{5.38}$$

The Fermi surface is defined as the locus of the peaks at energy $\epsilon = \epsilon_f$. Fig. 5.3 shows the BSF of $B2$ $CoMn_{0.5}Si_{0.5}$ sliced by the Γ-X×Γ-X plane (see Fig. 5.1) through the Fermi surface. It can be seen that at the Fermi surface, the BSF can still be considered to take the form of a Lorentizian, but instead of Γ representing the inverse lifetime, it can now be interpreted as the inverse of the mean free path of the electrons in real space,

$$\Lambda = \frac{1}{\Gamma}. \tag{5.39}$$

Since the conductivity, as suggested by Eq. (5.30), is directly proportional to the mean free path, a sharp BSF would indicate a high conductivity. Fig. 5.3 shows the spin up channel to have high conductivity because of the sharp BSF peaks, whereas

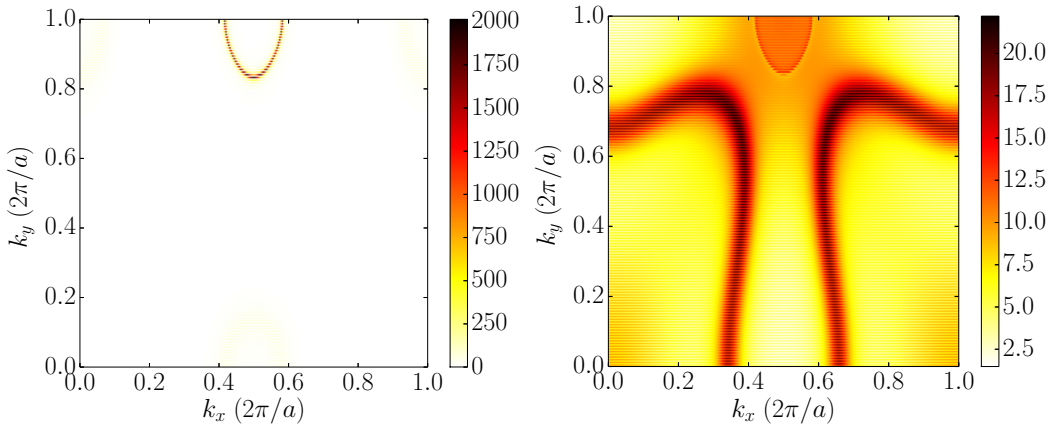


(a) Spin up (b) Spin down

Figure 5.3: BSF of $B2$ $CoMn_{0.5}Si_{0.5}$ sliced by the Γ-X×Γ-X plane (as indicated on Fig. 5.1) through the Fermi surface, where (a) shows spin up and (b) shows spin down.

the Mn-Si disorder has a large effect on the spin down channel and reduces the conductivity.

## 5.4 Fermi velocity

This section will continue the discussion from Chapter 4 to find the best candidates for HM. So again, the 5-components alloy of the form $CoFe_xMn_{0.5-x}Ga_ySi_{0.5-y}$ was constructed, but instead of using the DOS data, BSF data were simulated with different permutations of the concentrations. For each concentration, 10 even cuts by the Γ-X×Γ-X plane from $(\epsilon_f - 0.004)$Ry to $(\epsilon_f + 0.005)$Ry of BSF were simulated, where $\epsilon_f$ was taken to be 0.8652Ry for all the concentrations. Each cut gives pictures such as Fig. 5.3. The reason for the cuts at the Fermi level, $\epsilon_f$ is because it allows us to calculate quantities such as the velocity and the mean free path of the electrons at the Fermi surface. The small range of 0.01Ry around $\epsilon_f$ was chosen, because having a larger range may start to include other bands (this can be see from Fig. 5.2b), which will interfere with the calculations. Having a smaller range, we may not even observe changes with the BSF.

The velocity at the Fermi surface, known as the *Fermi velocity* was first analysed in the light of Eq. (5.30), since it states that the conductivity increases with the Fermi velocity. Recall the condition that a HM must only conduct electricity in one spin channel, so we are particularly interested at the minority spin where the band gap is and whether it has zero or at least close to zero Fermi velocity. The

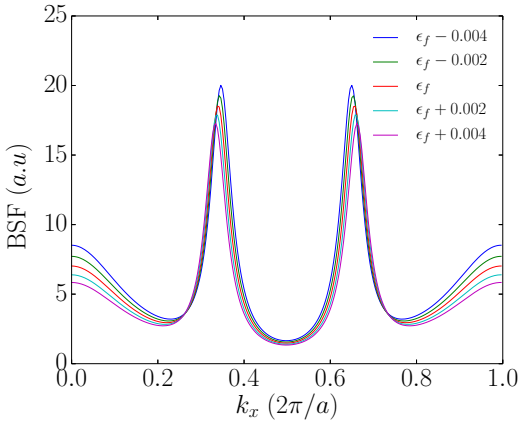


Figure 5.4: Minority spin BSF at $k_y = 0$ of $B2$ $CoMn_{0.5}Si_{0.5}$ sliced by the Γ-X×Γ-X plane through the Fermi surface at $\epsilon = (\epsilon_f - 0.004)$Ry, $(\epsilon_f - 0.002)$Ry, $\epsilon_f$Ry, $(\epsilon_f + 0.002)$Ry and $(\epsilon_f + 0.004)$Ry, shown by blue, green, orange, cyan and purple, respectively. This demonstrates how the BSF is moving outward from $k_x = 0.5$ as the energy increases.

Fermi velocity was calculated using

$$I_{v_f} = \frac{\Delta E}{\Delta k}, \tag{5.40}$$

where $\Delta E$ is the total change in energy (in this case, 0.01Ry) and $\Delta k$ is the total change in position of the peak that we are "tracking" in **k**-space. Note that the atomic units were used, hence $\hbar$ vanished from our calculation of the velocity.

In order to track the motion of the BSF, a much simplified approach was taken. Only the motion of a single strip of the BSF at $k_y = 0$ was considered. Fig. 5.4 is an example of this BSF at $k_y = 0$, where the movement is clearly shown by the different coloured plots. The problem was further simplified by having only one of the peaks tracked. This is done by cropping the data to only range from $k_x = 0$ to $k_x = 0.5$. Then $\Delta k$ is taken to be the absolute value of the difference in the position of the peak at $\epsilon = (\epsilon_f - 0.004)$Ry and $\epsilon = (\epsilon_f + 0.005)$Ry, i.e.,

$$\Delta k = \left| k_{\text{peak}}(\epsilon_f + 0.005) - k_{\text{peak}}(\epsilon_f - 0.004) \right|. \tag{5.41}$$

The cropping of the data and tracking only a single peak can be justified by the assumption that the BSF is symmetric at $k_x = 0.5$, which is shown by figures such as Fig. 5.3 and Fig. 5.4.

Fig. 5.5 shows the result of the calculations from the above procedure for the minority spin. This is a rather interesting result, as a pattern does emerge to

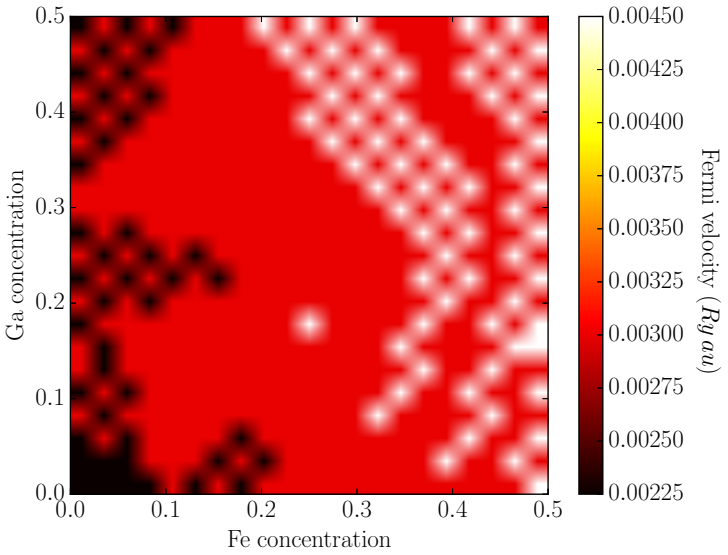


Figure 5.5: Fermi velocity analysis for minority spin. The lighter and darker region correspond to alloys with higher and lower Fermi velocity, respectively. Here, the darker region is the region of interest.

some extent, where low Fe concentration is more preferable. However, it can be seen that most values of the Fermi velocity are the same and the pattern only arises by some fluctuations of the calculation. It is therefore very hard to conclude, from our model, the correlation between the different concentrations and the Fermi velocity. This certainly showed the limitation of our simplification to the calculation. To improve this results, one can simulate much higher resolution of BSF data. The most accurate way to get the Fermi velocity, however, would be to sample the motion of the whole BSF as a function of energy, but this approach could not be used because the BSF does not contain enough information about the exact direction the carriers are travelling at different points. For example, the peak at $k_x = 0$ was found to be moving in the $k_y$ direction instead of $k_x$, as in our case.

This analysis was also applied to the majority spin, since the conductivity for this spin channel is also of importance as higher conductivity is more preferable for this spin channel. Instead of using a single strip of BSF at $k_y = 0$, the strip at $k_y = 1$ had to be taken because Fig. 5.3a clearly shows that the peaks for the majority spin is mainly situated at $k_y > 0.5$. Fig. 5.6 shows the result of the calculations for the majority spin. This is a very different result compared to the minority spin. A clear pattern emerges where the increase of Fe and Ga concentrations increases the Fermi velocity and hence the conductivity. This is can be explained by the fact that both Fe and Ga have higher conductivity than Si and Mn, respectively.

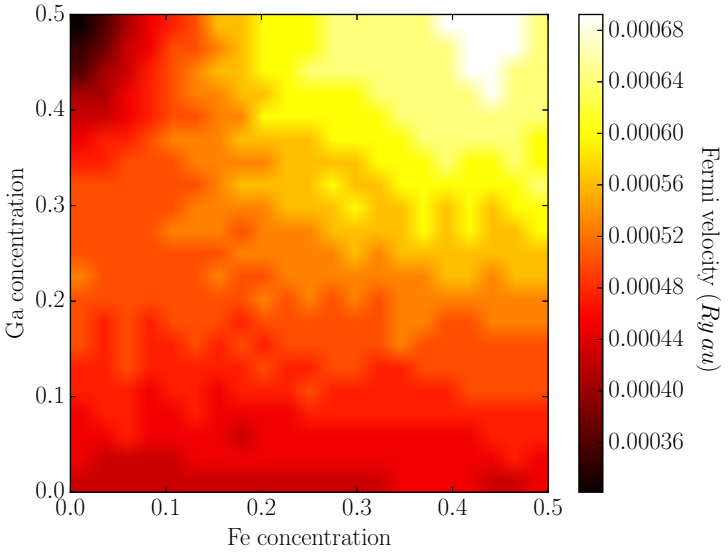


Figure 5.6: Fermi velocity analysis for majority spin. The lighter and darker region correspond to alloys with higher and lower Fermi velocity, respectively. Here, the lighter region is the region of interest.

## 5.5 Mean free path

To gain complete insite to the conductivity, the mean free path is also needed. As discussed in Chapter 5.3, the mean free path can be calculated by taking the FWHM, $\Gamma$ of the peaks of the BSF,

$$I_\Lambda = \frac{1}{\Gamma}. \tag{5.42}$$

The same BSF data detailed in the previous section was used for this calculation, including taking only a single strip of BSF at $k_y = 0$. We again assumed the symmetry and therefore only one of the peaks was considered. To calculate $\Gamma$, a Lorentzian, Eq. (5.37) was fitted using least squares fit to the BSF. However, Fig. 5.4 shows that smaller peaks are forming on the two sides, thus it can pose a problem with the fitting. In order to overcome this problem, further cropping of the data was done, such that the peak is positioned in the middle and the width of the data is the distance from the position of the original peak to $k_x = 0.5$ doubled. Fig. 5.7 shows the effect of the cropping and the Lorentzian fit. It can be seen that the cropping would still include part of the smaller peak formed on the left. As a result, the width of the Lorentzian is slightly larger than the data. Nonetheless, the difference is negligible.

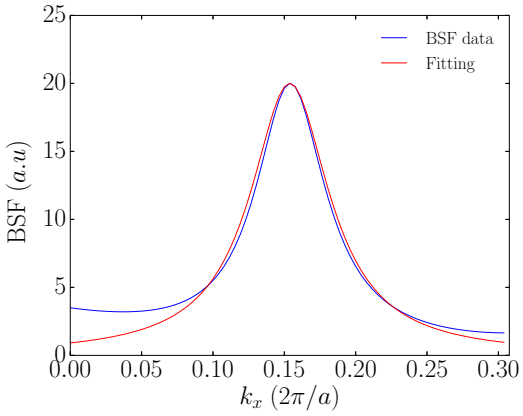


Figure 5.7: The cropped BSF from Fig. 5.4 at $\epsilon = \epsilon_f - 0.004$Ry. The BSF data and the fitting is shown in blue and red, respectively.

$\Gamma$ automatically arises from the fitting and hence the mean free path. The mean free path was calculated for the 10 slices of BSF at $\epsilon = (\epsilon_f - 0.004)$Ry to $\epsilon = (\epsilon_f + 0.005)$Ry and the average was taken to get the final value. We once again performed the calculations for both the minority spin and the majority spin. Fig. 5.8 shows the results for the minority spin. Since we are looking for small mean free path or small conductivity in this channel, it shows that increasing Ga concentration is not desirable, whereas it is insensitive to the increase of Fe concentration. This result is unexpected because from the band gap analysis in Chapter 4.1, it shows that the band gap would vanish for high Fe concentration, meaning that the conductivity would increase with the Fe concentration.

Fig. 5.9 also shows a rather unexpected results for the majority spin. It shows that it is more preferable to have low Fe and Ga concentrations. Although this seems to show the same correlation as the DOS analysis in Chapter 4, this shows a contrary result to the Fermi velocity analysis from the previous chapter, where the conductivity increases with the Fe and Ga concentrations. However, both problems from the minority spin and the majority spin might be related to the shift of the Fermi level. A more sophisticated approach could be employed by using the DOS data to correct the Fermi level, then calculate the BSF around the corrected Fermi level. Although it could again be caused by the simplification that only a single strip of the BSF was used, whereas the full BSF should be sampled instead.

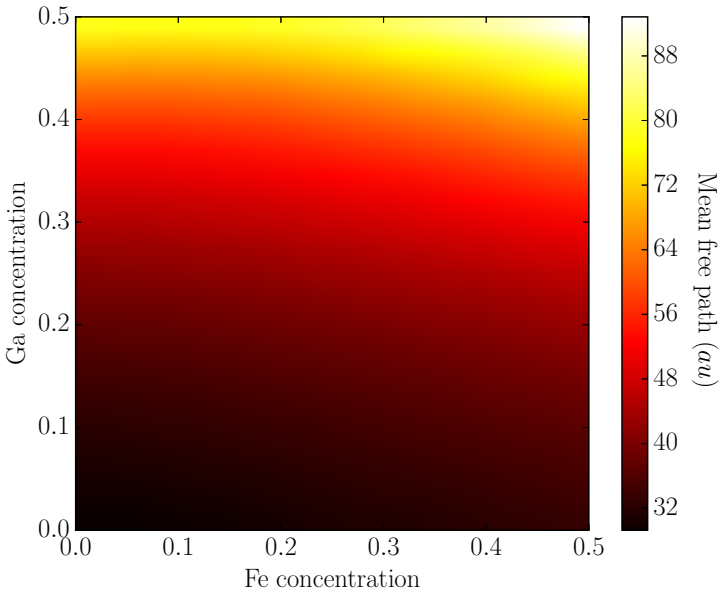


Figure 5.8: Mean free path analysis for minority spin. The ligher and darker region correspond to alloys with higher and lower mean free path, respectively. Here, the darker region is the region of interest.

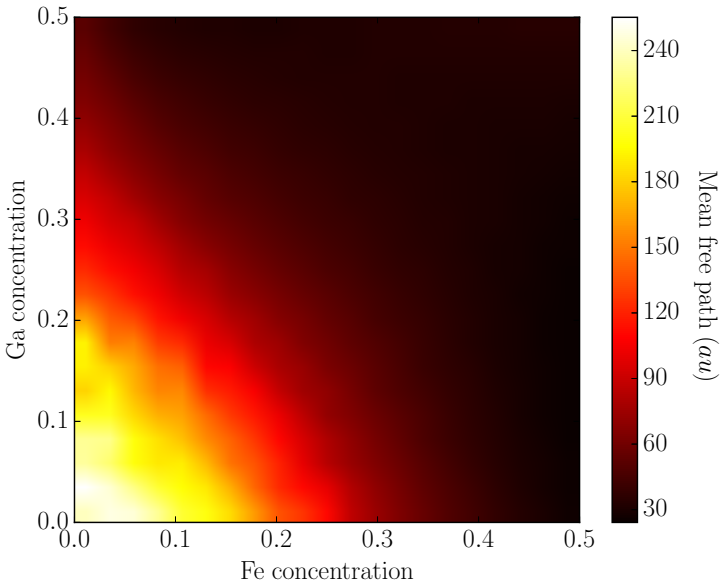


Figure 5.9: Mean free path analysis majority spin. The ligher and darker region correspond to alloys with higher and lower mean free path, respectively. Here, the lighter region is the region of interest.

# Chapter 6

# Candidates for Potential Half-metals

Fig. 6.1 shows the correlation between the concentrations and the half-metallicity of the $CoFe_xMn_{0.5-x}Ga_ySi_{0.5-y}$ alloys. It was calculated by summing the calculations from the band gap analysis in Chapter 4.1, DOS difference $\epsilon_f$ in Chapter 4.2 and the mean free path analysis in Chapter 5.5. They were assumed to be weighted evenly, thus using the rescaling method described in Chapter 4.3. Note that the result from the Fermi velocity calculations in Chapter 5.4 was ignored because it is not correlated.

It was found that the $B2$ $CoFe_{0.5}Ga_{0.5}$ was furthest from a HM. This result is consistent with the experimental work by Varaprasad *et al.* [10], in which they reported the $Co_2FeGa$ alloy in both $L2_1$ and $B2$ structures not to be a HM. In addition, we can see a similar trend from their spin polarisation calculations to some extent, that the low Fe and Ga concentrations are more preferable. For example, the $Co_2Mn(Ga_{0.25}Si_{0.75})$ was found to have spin polarisation of 0.63 and the increase of the Ga concentration to 1 would reduce the spin polarisation to 0.6, similarly with the increase of Fe concentration. As a surprise, though, the $Co_2MnSi$ and $Co_2(Mn_{0.5}Fe_{0.5})Ga$ shows a low and high spin polarisation, respectively, which is in contrast with our calculations. This could be caused by the effect of the $B2$ disordering, since their measurements were done for the $L2_1$ phase.

It must be emphasised that our calculations only illustrate the general trend for the effects of compositional disorder affect one spin channel more than the other which promotes HM behaviour, and not to calculate exactly which material is a HM. From Fig. 6.1, it is clear that the increase of the Fe or the Ga concentration would cause the half-metallicity to disappear, therefore the half-metallic property of

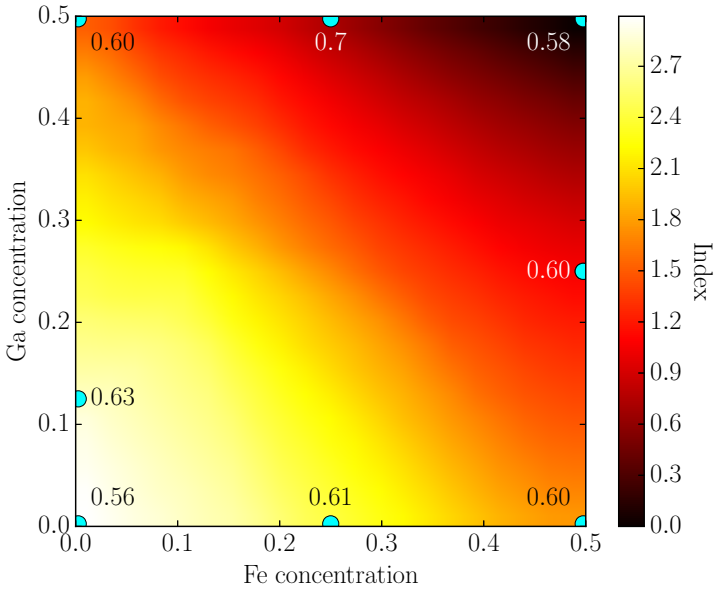


Figure 6.1: Combination of the band gap analysis, DOS difference at $\epsilon_f$ and the mean free path calculations, where higher index shows alloys with behaviour closest to a HM. The lighter region where the Ga and Fe concentrations are low is therefore the region of interest. Some related alloys in $L2_1$ phase measured by Varaprasad *et al.* [10] using the PCAR technique are also plotted along with their spin polarisation.

$CoFe_xMn_{0.5-x}Ga_ySi_{0.5-y}$ is more robust for low Fe and Ga concentrations. It can also be seen that the increase of Fe concentration can cause the HM behaviour to vanish quicker than the increase of Ga concentration.

# Chapter 7

# Conclusions and Outlook

In this thesis, we have presented the analysis of the half-metallicity of a new series of Co-based alloys with $B2$ disordering, $CoFe_xMn_{0.5-x}Ga_ySi_{0.5-y}$ ($0 < x < 0.5$, $0 < y < 0.5$). The 5-components alloys were investigated using *ab initio* calculations, where techniques were developed to extract the half-metallic properties from their DOS and BSF. In Chapter 4 we presented the first set of analyses using the DOS. The first method developed involves finding a spin down band gap through calculating the number of states around the Fermi level. The second method developed calculates the spin up-spin down difference at the Fermi level. These two methods at no stage assumes the accuracy of the DOS calculation. In fact, both methods were developed to only give a general overview of the correlation between the concentrations and the half-metallicity. Exact calculation of the band gap size and the spin polarisation were not used, therefore problems such as the band gap problem introduced by the LDA can be avoided. The analyses of the DOS alone show that the alloys with low concentrations of both Fe and Ga can be potential candidates for HM. Moreover, the half-metallicity drop more rapidly for the increase of Fe concentration compared to the increase of Ga concentration.

Another 2 methods of quantifying the half-metallicity from BSF were developed, which is outlined in Chapter 5. These two methods involves in finding the Fermi velocity and the mean free path from slices of the BSF at the Fermi level. As both quantities require much cunning to calculate accurately, simplification of the BSF was needed. The Fermi velocity calculations show the limitations of the simplification, where the correlation is not well defined. Due to this problem, the Fermi velocity calculations were not considered further. Although, the mean free path calculations show a better correlation, the correlation seems to be inconsistent with the band gap analysis, where the increase of Fe concentration should have

destroyed the band gap, thus increasing the mean free path, as its opposite in our case. Nevertheless, in Chapter 6 we have combined the calculations from the DOS analysis and the mean free path calculations to conclude that it is most desirable to have low concentrations of Fe and Ga for spintronics applications. This is indirectly supported by the experimental work done by Varaprasad *et al.* [10].

The use of the LDA for the exchange correlation functional is because it is fast and this thesis is not looking to give exact calculations of the half-metallic properties. Nonetheless, it is preferable to seek for better electronic structures calculations to support our conclusion. The problem with the shift of the Fermi level can be fatal in determining the half-metallicity, because the location of the band gap is a very important factor in HMs. There are many other approximation schemes which can provide significant improvement over LDA can be used, such as the generalised gradient approximation (GGA) [64, 65], GWA [55] and the self-interaction correction (SIC) method [66]. Using these methods will definitely improve the quality of the results. However, it must be stressed that attemts were made to reduce the limitations of the LDA and the analyses were designed to only give a general overview. The trends from all the analyses presented will change, but not drastically. Hence the conclusions will not necessarily change.

There are still plenty of scope for extensions of the methods. If possible, a more sophisticated approach which can remove the needs for the simplification of the BSF in order to calculate the transport properties would be favourable. The versatility of the methods developed in this thesis should be emphaised. It can be considered as general techniques to quantify half-metallicity and can be applied on to other alloys. To conclude, the analysis on multi-components alloys can provide experimentalists a framework to guide the growth of HM. Furthermore, the analytical methods developed in this thesis can spur new investigations into other compounds in the light of disovering new HMs.

# Bibliography


[1] A. K. T. Assis and K. H. Wiederkehr, *Weber's Planetary Model of the Atom*, edited by G. Wolfschmidt (Tredition, 2011).

[2] A. H. Wilson, *The Theory of Metals*, 2nd ed. (Cambridge University Press, 1965).

[3] L. Makinistian, M. M. Faiz, R. P. Panguluri, B. Balke, S. Wurmehl, C. Felser, E. a. Albanesi, a. G. Petukhov, and B. Nadgorny, Physical Review B **87**, 220402 (2013).

[4] R. D. Groot and F. Mueller, Physical Review Letters **50**, 2024 (1983).

[5] M. Katsnelson, V. Irkhin, L. Chioncel, A. Lichtenstein, and R. de Groot, Reviews of Modern Physics **80**, 315 (2008).

[6] I. Žutić, J. Fabian, and S. Sarma, Reviews of Modern Physics **76**, 323 (2004).

[7] P. Dederichs, Journal of Electron Microscopy **54**, 53 (2005).

[8] J. M. D. Coey and M. Venkatesan, Journal of Applied Physics **91**, 8345 (2002).

[9] Y. Miura, K. Nagao, and M. Shirai, Physical Review B **69**, 144413 (2004).

[10] B. Varaprasad, A. Srinivasan, Y. Takahashi, M. Hayashi, A. Rajanikanth, and K. Hono, Acta Materialia **60**, 6257 (2012).

[11] U. Geiersbach, A. Bergmann, and K. Westerholt, Journal of Magnetism and Magnetic Materials **240**, 546 (2002).

[12] R. Jones and O. Gunnarsson, Reviews of Modern Physics **61**, 689 (1989).

[13] W. Kohn and L. Sham, Physical Review **140**, A1133 (1965).

[14] J. Zabloudil, R. Hammerling, P. Weinberger, and L. Szunyogh, *Electron Scattering in Solid Matter* (Springer, Berlin, 2005).

[15] H. Ebert, D. Ködderitzsch, and J. Minár, Reports on Progress in Physics **74**, 096501 (2011).

[16] H. Ebert, "The Munich SPR-KKR package, version 6.3, http://ebert.cup.uni-muenchen.de/SPRKKR," (2012).

[17] R. Martin, *Electronic Structure: Basic Theory and Practical Methods*, 5th ed. (Cambridge University Press, New York, 2011).

[18] P. Hohenberg and W. Kohn, Physical review **136**, B864 (1964).

[19] E. Engel and R. M. Dreizler, *Density Functional Theory - An Advanced Course* (Springer, Berlin, 2011).

[20] O. Gunnarsson and B. Lundqvist, Physical Review B **13**, 4274 (1976).

[21] R. G. Parr and W. Yang, *Density-Functional Theory of Atoms and Molecules* (Oxford University Press, New York, 1989).

[22] J. Korringa, Physica **13**, 392 (1947).

[23] W. Kohn and N. Rostoker, Physical Review **94**, 1111 (1954).

[24] E. N. Economou, *Green's Functions in Quantum Physics*, 3rd ed. (Springer, New York, 2006).

[25] B. Lippmann and J. Schwinger, Physical Review **79**, 469 (1950).

[26] J. Zabloudil and P. Hammerling, Robert, Szunyogh, Laszlo, Weinberger, *Electron Scattering in Solid Matter* (Springer, New York, 2005).

[27] D. Fabian and L. Watson, *Band Structure Spectroscopy of Metals and Alloys* (Academic Press, New York, 1973).

[28] P. Lloyd and P. Smith, Advances in Physics **21**, 69 (1972).

[29] J. S. Faulkner and G. Stocks, Physical Review B **21**, 3222 (1980).

[30] N. F. Mott, Philosophical Magazine Series 7 **22**, 287 (1936).

[31] U. Mizutani, *Introduction to the Electron Theory of Metals* (Cambridge University Press, Cambridge, 2001).

[32] P. Soven, Physical Review **156**, 809 (1967).

[33] P. Soven, Physical Review B **2**, 4715 (1970).

[34] B. Gyorffy, Physical Review B **5**, 2382 (1972).

[35] H. Winter and G. Stocks, Physical Review B **27**, 882 (1983).

[36] P. J. Durham, B. L. Gyorffy, and A. J. Pindor, Journal of Physics F: Metal Physics **10**, 661 (1980).

[37] F. Heusler, Verhandlungen der Deutschen Physikalischen Gesellschaft **5**, 219 (1903).

[38] Y. Takamura, R. Nakane, and S. Sugahara, Journal of Applied Physics **105**, 07B109 (2009).

[39] C. Berthier, L.-P. Lévy, and G. Martinez, *High magnetic fields : applications in condensed matter physics and spectroscopy* (Springer, London, 2001).

[40] I. Galanakis, P. Mavropoulos, and P. H. Dederichs, Journal of Physics D: Applied Physics **39**, 765 (2006).

[41] W. Pickett, Physical Review Letters **77**, 3185 (1996).

[42] J. R. Hook and H. E. Hall, *Solid State Physics*, 2nd ed. (John Wiley & Sons, New York, 2010).

[43] I. Galanakis and P. Mavropoulos, Journal of Physics: Condensed Matter **19**, 315213 (2007).

[44] I. I. Mazin, Physical Review Letters **83**, 4 (1998).

[45] I. Maskery, *Spin densities in 4f and 3d magnetic systems*, Ph.D. thesis, University of Warwick (2013).

[46] F. Ono and H. Maeta, Journal de Physique Colloques **49**, 63 (1988).

[47] J. R. Cerda, P. L. de Andres, A. Cebollada, R. Miranda, E. Navas, P. Schuster, C. M. Schneider, and J. Kirschner, Journal of Physics: Condensed Matter **5**, 2055 (1993).

[48] P. Enghag, *Encyclopedia of the Elements: Technical Data - History - Processing - Applications* (Wiley, New York, 2004) p. 667.

[49] D. P. Rai, A. Shankar, and R. K. Thapa, International Journal of Computational Physical sciences **3**, 21 (2012).

[50] S. H. Vosko, L. Wilk, and M. Nusair, Canadian Journal of Physics **58**, 1200 (1980).

[51] T. Takeda, Zeitschrift für Physik B Condensed Matter **48**, 43 (1978).

[52] M. Meinert, C. Friedrich, G. Reiss, and S. Blügel, Physical Review B **86**, 245115 (2012).

[53] P. Hasnip, C. Loach, J. Smith, M. Probert, D. Gilks, J. Sizeland, K. Yoshida, M. Oogane, A. Hirohata, and V. Lazarov, Journal of the Magnetics Society of Japan **38**, 50 (2014).

[54] J. P. Perdew, International Journal of Quantum Chemistry **28**, 497 (2009).

[55] L. Hedin, Physical Review **139**, A796 (1965).

[56] J. J. Thomson, Philosophical Magazine Series 5 **44**, 293 (1897).

[57] P. Drude, Annalen der Physik **306**, 566 (1900).

[58] L. S. Lerner, *Physics for Scientists and Engineers, Volume 2* (Jones & Bartlett Learning, 1997).

[59] J. Willard Gibbs, "Elementary Principles In Statistical Mechanics," (1960).

[60] H. Ebert, A. Vernes, and J. Banhart, Solid State Communications **104**, 243 (1997).

[61] J. S. Faulkner, Progress in Materials Science **27**, 1 (1982).

[62] B. Wiendlocha, Physical Review B **88**, 205205 (2013).

[63] B. E. A. Gordon, W. E. Temmerman, and B. L. Gyorffy, Journal of Physics F: Metal Physics **11**, 821 (1981).

[64] J. P. Perdew and W. Yue, Physical Review B **33**, 8800 (1986).

[65] J. P. Perdew, Physical Review B **33**, 8822 (1986).

[66] J. P. Perdew, Physical Review B **23**, 5048 (1981).